Quasilinear-based simulations of bidirectional type III bursts

Bo Li,[1] Peter A. Robinson,[1] and Iver H. Cairns[1]

Received 4 April 2008; revised 1 June 2008; accepted 22 July 2008; published 3 October 2008.

[1] Quasilinear-based simulations are presented of bidirectional type III bursts that originate in the corona and are observed at Earth, assuming plasma emission. By extending a recent simulation model to more realistic three-dimensional source structures and including Langmuir collisional damping, dynamic spectra of both the normal-drifting (normal) and the reverse-slope-drifting (RS) bursts are simulated and studied in detail for realistic electron-release and coronal parameters. The radio flux, brightness temperature, frequency drift rate, and time duration of the bursts agree semiquantitatively with typical observations. The flux of $2f_p$ emission is significantly higher than that of f_p emission, which is below the noise thresholds of typical radio instruments. This is mainly because the f_p emission is strongly free-free absorbed and further damped by scattering off density fluctuations. The $2f_p$ emission is asymmetric between the normal and RS bursts, with the normal burst stronger and lasting longer than the RS burst, consistent with observations. This occurs primarily because of the downgoing beam being weaker, not faster, and narrower in velocity space than the upgoing beam, and because of stronger free-free absorption for the RS burst than for the normal burst, consistent with a semiquantitative theory. Furthermore, the RS burst terminates at frequencies lower than the maximum simulated, and the normal burst extends to lower frequencies not simulated because of computational limitations. Collisional damping reduces the Langmuir wave levels and consequently suppresses the flux levels and washes out the dynamic spectral structures associated with successive wave-wave interactions when the damping is switched off.

Citation: Li, B., P. A. Robinson, and I. H. Cairns (2008), Quasilinear-based simulations of bidirectional type III bursts, *J. Geophys. Res.*, *113*, A10101, doi:10.1029/2008JA013255.

1. Introduction

[2] Bidirectional type III bursts have been observed mostly in the decimetric and metric frequency ranges. They consist of a pair of bursts with a common frequency-time origin. One is a normal-drifting burst (the normal burst) that has negative frequency drift rate, and the other a reverse-slope-drifting burst (the RS burst) that has positive frequency drift rate [*Aschwanden et al.*, 1993, 1995b; *Xie et al.*, 2000].

[3] It is generally accepted that the pair of bursts result from a single acceleration event during a flare that simultaneously produces two electron beams from a common region in the corona: one beam, the upgoing beam, propagates upward from the Sun along open magnetic field lines, and the other, the downgoing beam, propagates downward toward the Sun. According to flare models, oppositely directed magnetic field lines are driven together because of coronal motions and magnetic reconnection takes place. Electrons at the reconnection site are accelerated because of the release of magnetic energy, and time-of-flight effects lead to the formation of beams when the electrons propagate along the magnetic field lines. The beams can propagate away from the Sun and/or toward the Sun, forming upgoing and/or downgoing beams, respectively. Along their paths the beams drive Langmuir waves at the local plasma frequency f_p, and some of these are converted via plasma emission into electromagnetic radiation, at the fundamental frequency f_p and/or its second harmonic $2f_p$ [*Benz*, 1993; *Aschwanden*, 2002].

[4] Bidirectional type III bursts may provide the most stringent geometric constraints on the acceleration region in flares. For instance, one can use the starting frequencies of the bursts to bracket the vertical extents of both an elementary acceleration region and the entire acceleration region in a flare, and infer the electron density therein [*Benz*, 1993; *Bastian et al.*, 1998; *Aschwanden*, 2002, and references therein]. In addition, correlations between bidirectional type III bursts and hard X-rays may also constrain the magnetic topology in a flare [*Aschwanden*, 2002].

[5] A well-studied semiquantitative theory of plasma emission for interplanetary type III bursts involves the following steps [*Robinson and Cairns*, 1998a, 1998b, 1998c]: step i, a beam generates primary Langmuir waves

[1]School of Physics, University of Sydney, Sydney, New South Wales, Australia.

0148-0227/08/2008JA013255

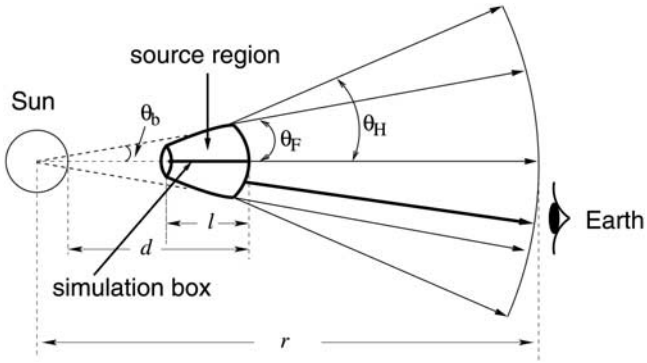

Figure 1. Schematic diagram showing the simulations (not to scale). The source region is three dimensional, which subtends a (varying) half-angle θ_b at the Sun, and has length l along its axis and radial distance d from the Sun. Within the source, the dynamics of beam, Langmuir waves, and ion-sound waves are simulated in one dimension along the axis of the 3-D source region, but radiation is simulated in three dimensions. At the end of the source region, rays subtend uniform cones of half-angles θ_F and θ_H at the Sun, for f_p and $2f_p$ emissions, respectively. The observer is at Earth, within the radiation cones, and the Earth-Sun distance r is much greater than d (so $r \gg d > l$). The arrows indicate that rays exiting the source region propagate in straight lines, with the thick arrow reaching the observer.

L by the bump-on-tail instability; step ii, L waves undergo electrostatic (ES) decay $L \rightarrow L' + S$ and generate product Langmuir waves L' and ion-sound waves S; step iii, S waves stimulate the L waves to produce fundamental (f_p) transverse waves F via electromagnetic (EM) decay $L \rightarrow F + S$; and step iv, L wave pairs coalesce to generate second harmonic ($2f_p$) transverse waves H via $L + L' \rightarrow H$. Generally, these beam-wave and wave-wave interactions can take place in the solar wind and in the corona, and they are assumed here to lead to bidirectional type III bursts. Other processes (e.g., scattering off ions, linear mode conversion, and electron cyclotron maser emission) are assumed to be less important [*Cairns*, 2000, 2004; *Mitchell et al.*, 2003, 2005; *Bastian*, 2004; *Raulin and Pacini*, 2005], and are not included. The type III system thus includes five elements: electron beam, ES Langmuir and ion-sound waves, and EM fundamental and second harmonic transverse waves.

[6] The above theory has been generalized to model bidirectional type III bursts [*Robinson and Benz*, 2000]. This model took into account the evolution of beams that are accelerated during flares, generation of Langmuir waves via quasilinear interactions, production of radiation via nonlinear wave-wave interactions in the source, and radiation propagation effects, which include scattering and free-free absorption. The model predicted dynamical evolution of emissivity as functions of source location and time, for electron acceleration on open and closed coronal field lines. However, numerical simulations of bidirectional type III bursts have not yet been reported.

[7] Recently, significant progress has been made in numerically modeling type III phenomena for normal bursts and associated sources, partly on the basis of quasilinear simulations for the dynamics of electrons and Langmuir waves [*Li*, 2007; *Li et al.*, 2008a, 2008b]. A novel model has been developed and applied to simulate a group of normal coronal type III bursts [*Li*, 2007], and a normal coronal type III burst [*Li et al.*, 2008a, 2008b]. The simulations agree semiquantitatively with typical observations. As illustrated by the schematic diagram in Figure 1 the simulation model includes the three-dimensional (3-D) structure of the source region, the dynamics in the source of the electron beam, Langmuir waves, ion-sound waves, fundamental and second harmonic radiation, and the propagation of radiation from the corona to interplanetary space. It yields the dynamic spectrum of radiation measured by a remote observer. In contrast, previous quasilinear calculations [e.g., *Takakura and Shibahashi*, 1976; *Magelssen and Smith*, 1977; *Grognard*, 1985; *Ziebell et al.*, 2001; *Kontar and Pecseli*, 2002; *Li et al.*, 2003] could only simulate the dynamic evolutions of electron beam, and Langmuir and ion-sound waves, not the radiation.

[8] In this paper we extend our recent work to simulate bidirectional type III bursts, focusing on the RS bursts driven by the downgoing beams and the differences between RS and normal bursts. We also generalize our earlier model to a more realistic 3-D source, include collisional damping of Langmuir waves for the first time. In this work, the angle θ_b subtended at the Sun by the 3-D source in Figure 1 increases with increasing source height (or decreasing frequency), to be consistent with observations [*Suzuki and Dulk*, 1985; *Leblanc et al.*, 2000]. In our earlier work, θ_b was assumed to be constant, and collisional damping of Langmuir waves was neglected [*Li*, 2007; *Li et al.*, 2008a, 2008b]. The emphases of this work are on detailed comparison of the spectral characteristics predicted for the RS and normal bursts, on detailed first comparisons of these predictions with typical observations for bidirectional type IIIs, and on understanding these characteristics by detailed study of the beam and wave dynamics in the source.

[9] The paper is organized as follows. In section 2, we review the simulation model developed in our previous work and extend it to a more general 3-D source geometry and include collisional damping of Langmuir waves. Section 3 presents the simulated dynamic spectra and the dynamics of beam and waves in the source region, where detailed comparisons for spectral characteristics between simulations and observations are made. This is followed by demonstrating the effects of varying beam parameters and coronal conditions on the simulated dynamic spectra in section 4. Section 5 is devoted to discussions of the implications and limitations of the simulations. Finally, section 6 summarizes the results.

2. Simulation Model

[10] The original simulation model for this work was presented recently [*Li*, 2007; *Li et al.*, 2008a] and is summarized in Appendix A. Here we briefly outline the model and focus on the new developments in this work.

[11] In the original model, the following approximations and assumptions were made:

[12] 1. The 3-D source region is a conical frustum volume of half-angle θ_b (or solid angle Ω_b) with its apex at the Sun, and its end is distance d from the Sun, and the

1-D simulation box is its symmetric axis of length l, where $\theta_b \ll 90°$.

[13] 2. The interactions in steps ii–iv in section 1, and the 3-D ES wave spectra are symmetric about the axis formed by the 1-D box (the magnetic field direction), with the 3-D ES wave spectra being constructed from the simulated 1-D spectra for an assumed angular distribution [*Li et al.*, 2005a, 2005b].

[14] 3. The source radiation is produced simultaneously and uniformly across a given layer (at location x, where $d - l \le x \le d$) of the source region.

[15] 4. Scattering of EM radiation off small-scale density fluctuations isotropizes the radiation pattern and broadens the angular range of radiation [*Steinberg et al.*, 1971; *Riddle*, 1974] such that at the end of the source region rays subtend a uniform cone of half-angle θ_T (or solid angle Ω_T) at the Sun, where $T = F$ or H [*Robinson and Cairns*, 1998a, 1998b]. In addition, scattering leads to a time delay [*Steinberg et al.*, 1971; *Riddle*, 1974; *Robinson and Cairns*, 1998a; *Robinson and Benz*, 2000] and damping [*Ginzburg*, 1964; *Robinson and Cairns*, 1998a; *Robinson and Benz*, 2000] for the f_p emission seen by a remote observer. The time delay is assumed to follow an exponential decay with a time constant t_d, which is defined by equation (42) of *Li et al.* [2008a].

[16] 5. The observer is at Earth, within the radiation cone, and the Earth-Sun distance r is much greater than d (so $r \gg d > l$). Thus the difference in propagation time between different locations in the last layer and the observer due to the finite angular extent of the source region is negligible.

[17] 6. Radiation propagates at the average group speed ($<c$) within the source region, taking into account the average effects of refraction and reflection, and at c once outside the source region. Here c is the speed of light.

[18] 7. For $2f_p$ emission, only radiation produced in the anti-sunward hemisphere (in wave vector space) is considered. Sunward-directed emission is neglected because the observer is at Earth and the reflected $2f_p$ emission from the sunward-directed radiation is expected to be weak [*Riddle*, 1974; *Robinson and Cairns*, 1998a, 1998b]. However, for f_p emission, both sunward-directed and anti-sunward-directed radiation is included because of nearly immediate reflection of f_p radiation produced in the sunward hemisphere [*Riddle*, 1974; *Li et al.*, 2006b].

[19] 8. Radiation losses by free-free absorption is taken into account, but losses by other wave-wave processes (e.g., $F \rightarrow L + S$) are neglected [*Robinson and Cairns*, 1998a; *Robinson and Benz*, 2000].

[20] By including the 3-D source character, and effects of refraction, reflection, scattering, and free-free absorption, the radio flux $\mathcal{F}_T$ measured by the observer due to radiation from a finite layer of the 3-D source in Figure 1 was first calculated and is given by (A11). The dynamic spectrum at the observer was then obtained by summing the above flux over source locations and simulation times, and is given by (A12). The characteristics of type III bursts calculated are: brightness temperature T_b (equation (19) of *Li et al.* [2008a]), frequency drift rate df/dt, and half-power time duration t_D.

[21] One new development of this work is that the assumption of constant θ_b of *Li* [2007] and *Li et al.* [2008a] has now been replaced with a more realistic model in which θ_b varies along the simulation box. Here θ_b increases with increasing source height (or decreasing frequency), and is approximated via [*Dulk*, 2000; *Leblanc et al.*, 2000]

$$\theta_b \approx \sin^{-1}\left[\left(\frac{r}{x + R_\odot} - 1\right)\sin\theta_o\right], \tag{1}$$

$$\theta_o = 4.2 \times 10^5 f^{-0.86}, \tag{2}$$

where θ_b and θ_o are in degrees, f in Hz, $f = f_p(x)$, and $R_\odot$ is the solar radius.

[22] Another improvement to our previous model [*Li*, 2007; *Li et al.*, 2008a] is that damping of Langmuir waves by electron-ion collisions is now included. In the quasilinear equation (A14) for Langmuir waves the collisional damping rate γ_c is given by [*Benz*, 1993]

$$\gamma_c = 3.04 \times 10^{-6} n T_e^{-3/2} \ln\Lambda, \tag{3}$$

where

$$\ln\Lambda = 22.8 + \ln T_e - 0.5 \ln n, \tag{4}$$

where γ_c is in s^{-1}, n is the electron number density in m^{-3}, and T_e is the electron temperature in K.

3. Results for Representative Parameters

[23] We show here simulation results using realistic coronal and beam acceleration parameters from observations, as summarized in Table 1. The coronal conditions are described via an isothermal atmosphere at $T_e = T_i = 2$ MK, whose density varies according to the 10 × Baumbach-Allen model [*Baumbach*, 1937; *Allen*, 1947] in order to represent an active region in the corona [*Hughes and Harkness*, 1963; *Benz et al.*, 1983; *Paesold et al.*, 2001]:

$$n(\bar{r}) = 10 \times 10^{14}\left(\frac{2.99}{\bar{r}^{16}} + \frac{1.55}{\bar{r}^{6}} + \frac{0.036}{\bar{r}^{1.5}}\right) \mathrm{m}^{-3}, \tag{5}$$

where $\bar{r} = r/R_\odot$. The beam acceleration parameters are as follows [*Aschwanden et al.*, 1995a, 1995b; *Aschwanden*, 2002; *Klein et al.*, 2005]: $T_h = 25$ MK, $t_0 = 5 \times 10^{-2}$ s, $\delta t = 2 \times 10^{-3}$ s, $x_0 = 0.13$ Gm (such that $f_p(x_0) = 250$ MHz), and $\delta x = 10^{-3}$ Gm. We choose $F_{acc} = 5 \times 10^{-5}$, similar to our earlier work [*Li et al.*, 2006a, 2008b; *Li*, 2007], except that here heating occurs for both $v > 0$ and $v < 0$, leading to the formation of both upgoing and downgoing beams.

[24] For the ES angular spectra described by (A17) we choose $\beta = 10$, corresponding to a characteristic angular spread of $\Theta = 26°$, following our previous work [*Li et al.*, 2006b]. We assume further that the radiation cones at the observer have half-angles $\theta_F = 30°$ and $\theta_H = 90°$, on the basis of a theory that is consistent with observational data [*Robinson and Cairns*, 1998a, 1998b; *Robinson and Benz*, 2000]. These are used in (A2) via the solid angle Ω_T. Figure 2 shows the variation of θ_b with source location in the spatial range simulated.

Table 1. Summary of the Simulation Parameters in Section 3 for the Coronal Conditions, Beam Acceleration, Radiation Source, Angular Spectra of ES Waves, and Radiation Propagation[a]

Parameter	Value	Unit
	Coronal Conditions	
T_e	2	MK
T_i	2	MK
$\Delta n/n$	7%[b]	—
	Beam Acceleration	
T_h	25	MK
F_{acc}	5×10^{-5}[c]	—
t_0	5×10^{-2}	s
δt	2×10^{-3}	s
x_0	0.13	Gm
δx	10^{-3}	Gm
	Radiation Source	
l	0.18[d]	Gm
d	0.25	Gm
	Angular Spectra of ES Waves	
β	10[e]	—
	Radiation Propagation	
θ_F	30°[f]	—
θ_H	90°[f]	—

[a]Based on observations [*Aschwanden et al.*, 1995b; *Aschwanden*, 2002; *Klein et al.*, 2005] unless otherwise specified.
[b]Value chosen on the basis of *Robinson and Cairns* [1998a, 1998c] for the predicted t_d to be consistent with observations.
[c]Value chosen similar to *Li et al.* [2006b] and *Li* [2007].
[d]Value chosen for the size of the 1-D simulation box in Figure 1.
[e]Value chosen similar to *Willes et al.* [1996] and *Li et al.* [2006b].
[f]Value chosen on the basis of *Robinson and Cairns* [1998a] to be consistent with observations.

[25] To evaluate f_p emission scattering off density fluctuations, two density fluctuation parameters are required: the r.m.s. level Δn and mean length scale l_{den}. Since no observational data are available for density fluctuations in the coronal regions of interest here ($1.10 \leq \bar{r} \leq 1.36$), we assume that the fluctuations have the same r.m.s. level $\Delta n/n = 7\%$ as in the work of *Robinson and Cairns* [1998c] and *Robinson and Benz* [2000]. The mean length scale of the fluctuations is

$$l_{den}(r) = 10^6 (r/1\ \mathrm{AU})^{1.61} \mathrm{m}, \tag{6}$$

which has the same scaling of l_{den} with r as in the work of *Robinson and Cairns* [1998c] and *Robinson and Benz* [2000], but is smaller by a factor about 12 than in the work of *Robinson and Cairns* [1998c] and *Robinson and Benz* [2000]. This occurs because of two reasons: first, the density model (5) used here is different from that of *Robinson and Cairns* [1998c], and, second, so that the calculated time constant $t_d(f)$ for f_p emission at the observer is consistent with observations.

[26] Note that the actual parameters for a specific bidirectional type III burst event may differ from the above, so our aim here is to demonstrate that simulations of bidirectional type III bursts using these realistic parameters yield good agreement with typical observations. The effects of varying parameters are discussed in section 4.

3.1. Dynamic Spectrum

[27] Here we study the radiation dynamic spectrum measured by a remote observer at Earth, The emphasis is on detailed comparisons of the characteristics of the normal burst and the RS burst.

[28] Figure 3 shows the dynamic spectra of f_p and $2f_p$ emissions predicted at Earth. The radio emission at the observer in Figures 3a and 3b is due to propagation of the F and H waves generated in the source via EM decays $L_0 \rightarrow F_1 + S_\theta$ and $L_1 \rightarrow F_2 + S_\theta$, and coalescences $L_0 + L_1 \rightarrow H_1$, $L_0 + L_\theta \rightarrow H_1$, and $L_1 + L_\theta \rightarrow H_2$, respectively. These processes involve beam-driven Langmuir waves L_0 and product Langmuir waves L_1 from the ES decay $L_0 \rightarrow L_1 + S_\theta$, where the subscript θ indicates that the corresponding waves are thermal. Further details are given in section 3.3.

[29] Figures 3a and 3b show the following features:

[30] 1. The $2f_p$ radiation flux is several orders of magnitude higher than that of f_p emission, with the latter unobservable for typical radio instruments.

[31] 2. The $2f_p$ and f_p emissions with negative drift rates are stronger by about one order of magnitude than those with positive drift rates.

[32] 3. The $2f_p$ emission with negative drift rates appears to continue to lower frequencies (higher altitudes) than simulated, where of course it will terminate eventually. The $2f_p$ emission with positive drift rates terminates within the simulated frequency range. Here radiation is regarded as terminated if its flux levels are much less than 10^{-22} W m^{-2} Hz^{-1} (i.e., 1 solar flux unit, or 1 sfu).

[33] 4. The emissions with negative drift rates start earlier than the emissions with positive drift rates.

[34] 5. At given frequencies symmetric about the central heating frequencies f_{F0} and f_{H0}, the emissions with negative drift rates start earlier, and last longer than the emissions with positive drift rates, where $f_{F0} \equiv f_p(x_0) = 250$ MHz and $f_{H0} \equiv 2f_p(x_0) = 500$ MHz.

[35] 6. The f_p emission shows long, exponential tails.

[36] These features of Figure 3 are consistent qualitatively with observations and theory [*Aschwanden et al.*, 1993, 1995b; *Robinson and Benz*, 2000]. The physics of these features is elaborated in the following paragraphs.

[37] The f_p flux levels are relatively lower than the $2f_p$ flux levels because f_p emission in the source is weaker and damping during propagation is stronger. We found in our recent simulations of normal coronal type III bursts [*Li*,

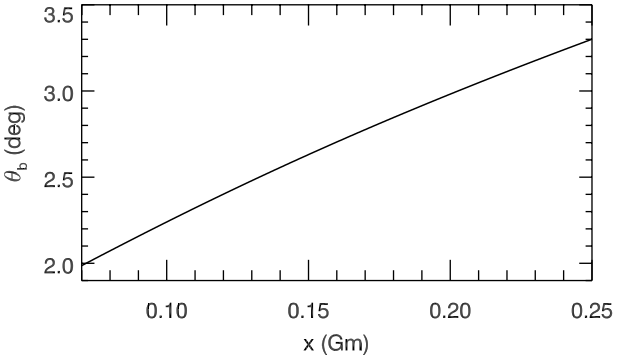

Figure 2. Variation with source distance x of the half-angle θ_b of the source region.

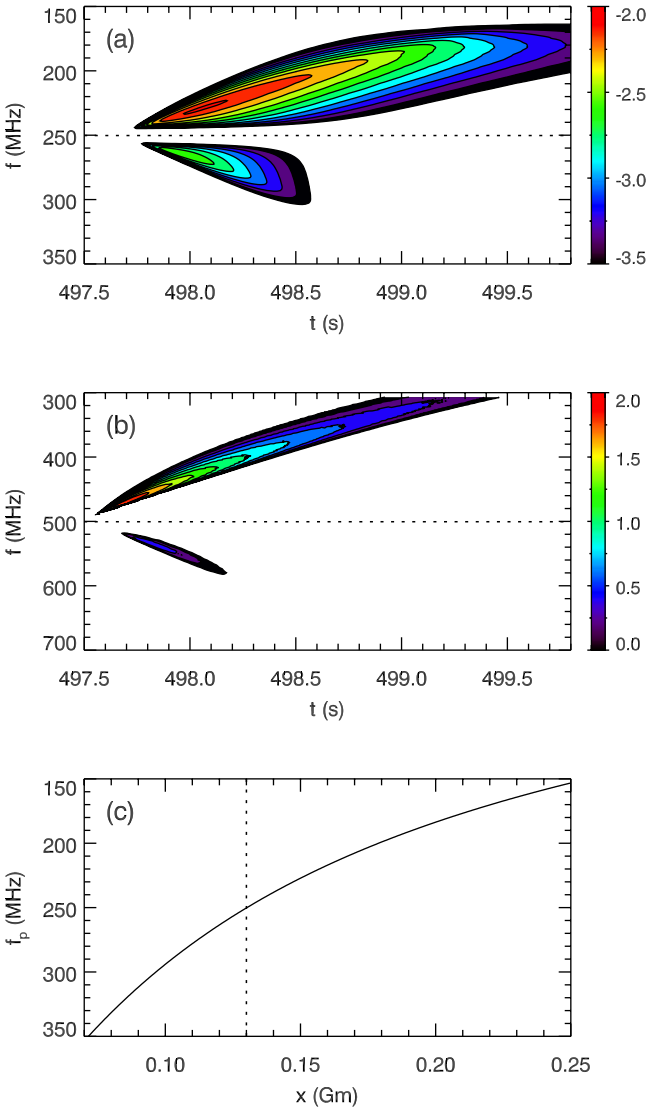

Figure 3. Predicted dynamic spectra at Earth for (a) f_p and (b) $2f_p$ radiation, in $\log_{10}[\mathcal{F}/(10^{-22}$ W m^{-2} Hz$^{-1})]$, and (c) variation of f_p with height. Dotted lines show the central frequencies f_{F0} and f_{H0}, or the central location x_0 of the heating. Note that the gray scales in Figures 3a and 3b are different.

2007; *Li et al.*, 2008b] that f_p emission is only weakly generated in the source since the ion-sound waves participating in the processes $L_0 \rightarrow F_1 + S_\theta$ and $L_1 \rightarrow F_2 + S_\theta$ are thermal. Moreover, f_p emission is strongly damped during propagation by free-free absorption and scattering off density fluctuations, the latter also leading to the exponential decay of the f_p flux. For $2f_p$ emission, free-free absorption is relatively weak, and losses by other mechanisms are neglected in our model. Therefore, $2f_p$ emission dominates in bidirectional type III bursts, consistent with observations [*Aschwanden et al.*, 1995b] and previous theoretical predictions [*Robinson and Benz*, 2000]. Since f_p emission appears unobservable, from now on we focus on $2f_p$ emission only, and refer to the $2f_p$ emission with negative drift rates as the normal burst, and the $2f_p$ emission with positive drift rates as the RS burst.

[38] The asymmetry between the normal and RS bursts is due mainly to the downgoing beam narrowing in velocity space and weakening relative to the background plasma, consistent with theoretical predictions [*Robinson and Benz*, 2000]. This effect is examined in detail in sections 3.2 and 3.3. In addition, the RS burst suffers more losses than the normal burst because of stronger free-free absorption during propagation.

[39] The flux of the normal burst in Figure 3b increases with decreasing frequency before it reaches a peak value at $f_H^N \approx 460$ MHz, and then decreases with decreasing frequency, similar to our predictions for normal coronal type III burst at lower frequencies [*Li et al.*, 2008b]. The flux of the RS burst varies similarly, except that it falls below typical instrument thresholds (e.g., $\leq 10^{-22}$ W m^{-2} Hz^{-1} for Phoenix [*Aschwanden et al.*, 1995b]) at $f_H^{RS} \approx$ 580 MHz. Figure 3b shows further that the normal burst will terminate at larger heights than simulated. The trends of the flux variation with f for both the normal and RS bursts are consistent qualitatively with observations [*Aschwanden et al.*, 1995b].

[40] The earlier onset of the normal burst than the RS at frequencies symmetric about f_{H0} occurs because first, the upgoing beam and the downgoing beam start from the same heating region, with the former moving toward, and the latter away from, the observer, and so second, the radiation generated by the upgoing beam travels a shorter path and so takes less time to reach the observer than the radiation associated with the downgoing beam. The longer duration of the normal burst than the RS burst at symmetric frequencies is because the upgoing beam and hence associated Langmuir waves last longer than the downgoing beam and linked Langmuir waves, as discussed in further detail in sections 3.2 and 3.3.

[41] Figure 4 shows in more detail the characteristic properties of the simulated dynamic spectrum: peak flux, brightness temperature, peak time of radio emission, frequency drift rate, and duration, of the normal and RS bursts. We see from Figure 4a that for both normal and RS bursts the peak flux increases rapidly after burst onset, reaches a maximum and then decreases slowly as the beams move away from the heating region. The normal burst has a peak flux about 9×10^{-21} W m^{-2} Hz^{-1}, nearly 25 times larger than that of the RS burst. Statistical analysis of 160 well-isolated type III bursts covering a frequency range of 100 – 3000 MHz, which include normal, RS and bidirectional bursts, shows that the peak flux of the weakest bursts is about 5×10^{-22} W m^{-2} Hz^{-1}, and only a few reach fluxes above 10^{-20} W m^{-2} Hz^{-1} [*Meléndez et al.*, 1999]. Thus the simulated peak fluxes are consistent quantitatively with the observations.

[42] Figure 4a also shows that there exists a frequency separation of $\delta f_H \approx 30$ MHz between the normal and RS bursts. The value of δf_H is consistent quantitatively with observations that about half of a study of 42 type III bursts, which include 10 bidirectional burst pairs, start within 40 MHz of a central frequency (610 MHz) [*Aschwanden et al.*, 1993]. This gap occurs because of the minimum distances required for formation of beams, and further requirements on the enhancement of Langmuir waves and onsets of nonlinear wave-wave interactions, as discussed by *Robinson and Benz* [2000]. The gap is asymmetric about

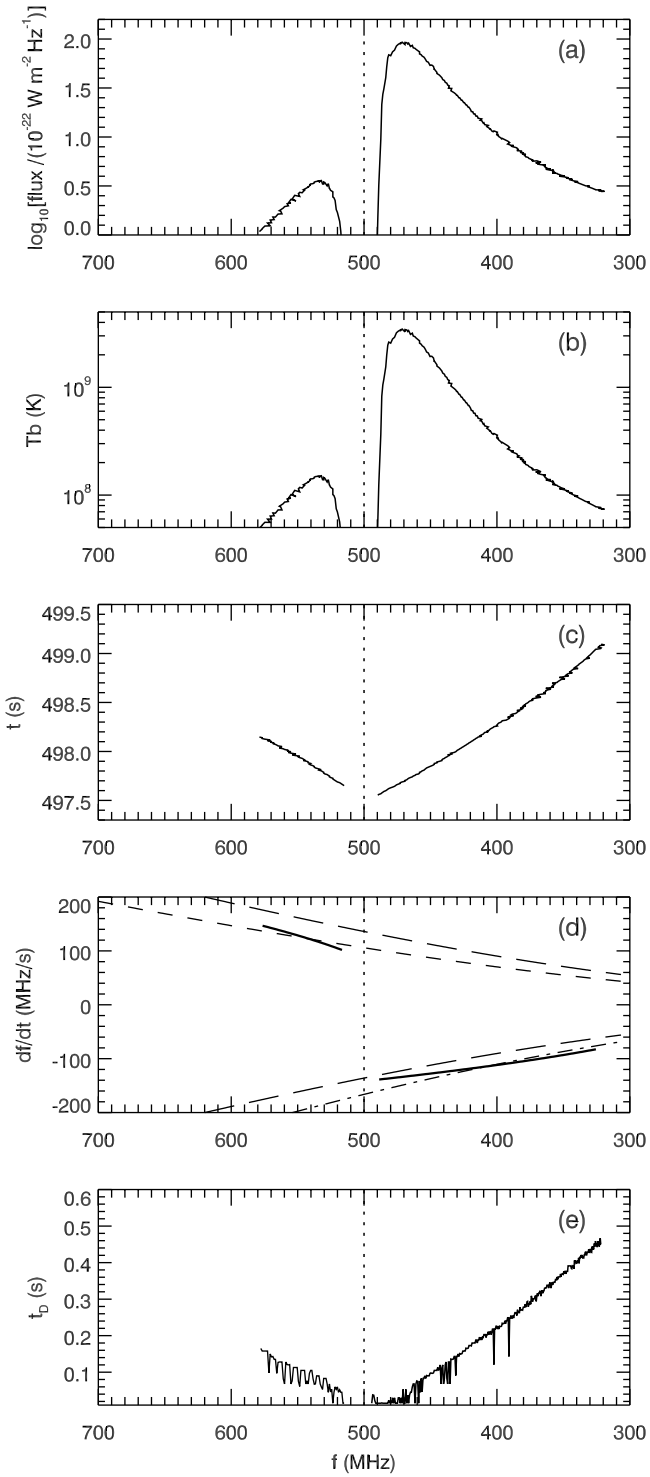

Figure 4. Variations with frequency of the (a) peak flux, (b) brightness temperature, (c) peak time of radio emission, (d) frequency drift rate, and (e) duration of the simulated $2f_p$ emission in Figure 3b. Dotted lines show the central heating frequency f_{H0}. Dashed, long-dashed, and dot-dashed curves are from the relation (7) with $\overline{v_b} = 0.14c$, $0.18c$, and $0.22c$, respectively. In Figure 4e the noisy dips for $390 \lesssim f \lesssim 480$ MHz and the irregular variation with f for $520 \lesssim f \lesssim 580$ MHz are due to the limited time resolution of the radio flux.

f_{H0}, with a smaller separation of about 10 MHz between the onset frequency and f_{H0} for the normal burst than the separation of about 18 MHz for the RS burst.

[43] Figure 4b shows that the brightness temperature T_b varies similarly to the peak flux in Figure 4a, and that the maximum T_b of both bursts occur at frequencies near where the radio flux peaks. We see from Figure 4b that T_b varies between about 5×10^7 K and 3.5×10^9 K for the normal burst, and 5×10^7 K and 1.5×10^8 K for the RS burst. To our best knowledge, no observational data of T_b exist that are directly available for comparison with the simulated T_b in the frequency range (300 MHz to 700 MHz) studied here. However, VLA observations have shown that the brightness temperature at 333 MHz varies between about 2×10^7 K and 3.5×10^8 K for a solar radio burst either of type III or type IV, where the uncertainty in distinguishing between type III and type IV was due to the poor temporal and spectral resolutions of the VLA [*Willson*, 1993]. Therefore, the simulated T_b is not inconsistent with these observations.

[44] Figure 4c shows the peak time of radio emission (or frequency-time drift) for the simulated event. We see that at onset the RS burst lags behind the normal burst by about 0.1 s. This time lag is consistent quantitatively with observations of 25 pairs of bidirectional bursts, which were found to start simultaneously (within the instrument time resolution of 0.1 s) [*Aschwanden et al.*, 1995b].

[45] We see from Figure 4c that by extrapolating the pair of oppositely drifting bursts, it appears that the paired bursts originate from a common frequency f_c, which is ≈495 MHz, and so is very close to the central heating frequency f_{H0} = 500 MHz. The minor difference between f_c and f_{H0} is due to the almost symmetric frequency-time drift profiles about f_{H0} for the paired bursts. The extrapolated intersection time for the paired bursts is $t \approx 497.5$ s, and so is about 497.45 s later than the central heating time $t_0 = 0.05$ s. The delay is due mainly to the radiation's propagation time from the source to the observer.

[46] The burst drift rate in Figure 4d shows negative and positive frequency drifts for the normal and RS bursts, respectively, as expected. (Here the drift rate is obtained by using the least-square fitted curves of the simulated frequency-time drift profiles in Figure 4c.) We see that $|df/dt|$ decreases with decreasing f and lies in the range 100–150 MHz s^{-1} for 520–580 MHz, and 80–130 MHz s^{-1} for 320–480 MHz, for the RS and normal bursts, respectively. The range of observed $|df/dt|$ shows wide scatter from burst to burst. For instance, for the set of bursts analyzed by *Meléndez et al.* [1999], $|df/dt|$ varies between about 150 MHz s^{-1} and 2500 MHz s^{-1} at ∼600 MHz for normal bursts, and is about 700 MHz s^{-1} for a RS burst at about the same frequency. For a set of 233 type III bursts that includes 30 pairs of bidirectional bursts in the range of 300–3000 MHz, df/dt is in the range about 160–1000 MHz s^{-1} for normal bursts at ∼300 MHz, and $|df/dt|$ in the range 200–1300 MHz s^{-1} for RS bursts at ∼600 MHz [*Aschwanden et al.*, 1995b]. A direct drift rate measurement for a pair of normal-RS bursts starting near 250 MHz shows that $|df/dt|$ is about 50 MHz s^{-1} for the RS burst within $230 \lesssim f \lesssim 250$ MHz, and about 70 MHz s^{-1} for the normal burst within $250 \lesssim f \lesssim 270$ MHz [*Xie et al.*, 2000]. Therefore the simulated burst drift rates are consistent quantitatively with, and lie near the lower limit of, observations.

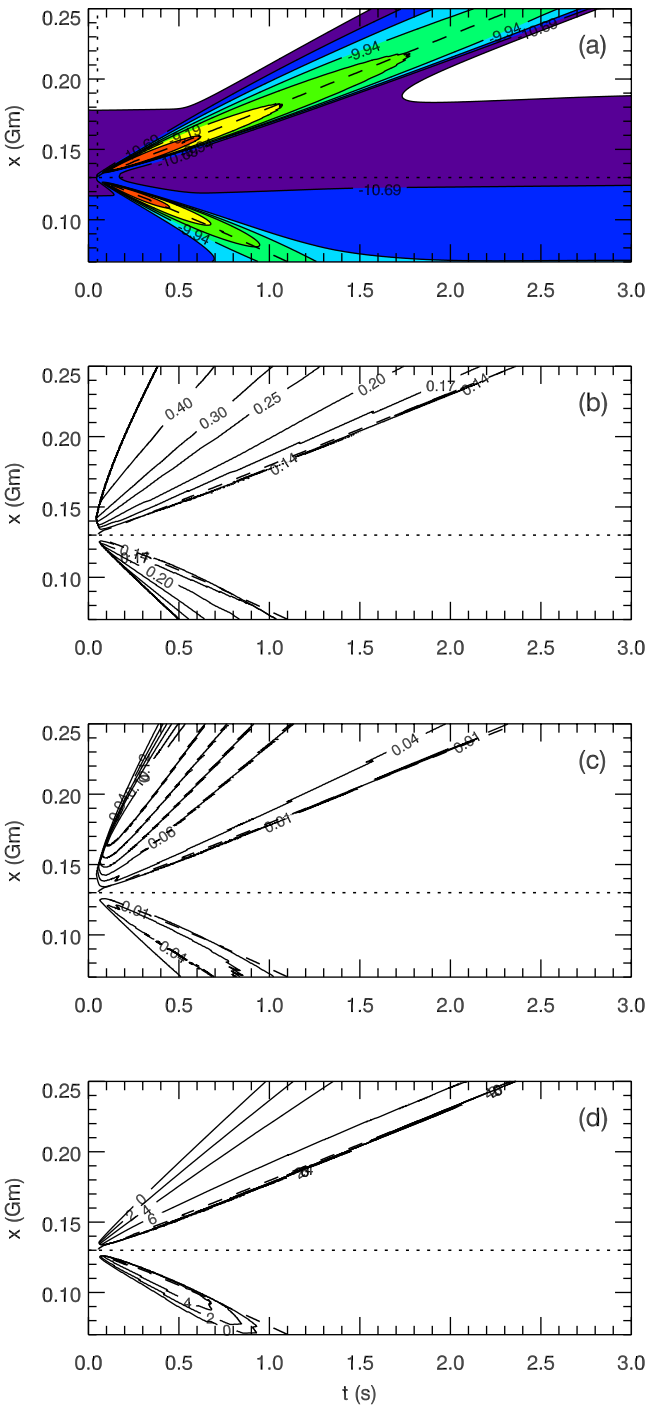

Figure 5. Variations with t and x of the (a) Langmuir wave energy density $\log_{10}[W/(1\ \mathrm{Jm}^{-3})]$, (b) beam speed v_b/c, (c) beam width $\Delta v_b/c$, and (d) beam number density $\log_{10}[N_b/(1\ \mathrm{m}^{-3})]$. Dotted lines in Figures 5a–5d show the central locations x_0, and in Figure 5a the central time t_0, of the heating. The dashed curves in Figures 5a–5d show the trajectory of maximal Langmuir energy density, which evolves at a mean beam speed $\langle v_b \rangle \approx 0.18c$.

[47] In the plasma emission scenario, for a given density model, there exists a quantitative relation between the frequency drift rate and beam speed [e.g., *Wild*, 1950; *Hughes and Harkness*, 1963; *Alvarez and Haddock*, 1973; *Mann et al.*, 1999; *Klassen et al.*, 2003]. In its simplest form, the relation can be written as

$$\frac{df}{dt} = \frac{\overline{v_b}}{2n}\frac{dn}{dr}f. \tag{7}$$

To derive (7), the following assumptions are made: the beam moves radially at an average, constant speed $\overline{v_b}$; rays propagate at a constant speed (i.e., c); and radiation propagation effects are negligible. The drift rates predicted by (7) for the density model (5) and assumed values $\overline{v_b} = 0.14c$, $0.18c$, and $0.22c$ are also shown in Figure 4d. We see from Figure 4d that the simulated drift rate agrees semiquantitatively with the prediction (7) if it is assumed that $\overline{v_b} \approx 0.14c$ for the RS burst, and $\overline{v_b} \approx 0.22c$ for the normal burst. In fact, the actual beam speeds for significant enhancement of Langmuir waves vary between about $0.1c$ and $0.3c$, which are derived from the dynamics of beam and Langmuir waves in section 3.3.1. Thus the relation (7) holds semiquantitatively for both the normal and RS bursts with the physical beam speeds, and indicate that, on average, the downgoing beam is slower than the upgoing beam.

[48] Figure 4e shows the variation of burst duration t_D with frequency. We see clearly that the RS burst has shorter t_D than the normal burst, with $t_D \gtrsim 0.02$ s near the onset of both bursts and $t_D \approx 0.5$ s for the normal burst at the end of simulation. These simulated t_D are consistent quantitatively with observations of $0.2 \lesssim t_D \lesssim 0.5$ s for $300 \lesssim f \lesssim 600$ MHz [*Meléndez et al.*, 1999], where the observational data were fitted with Gaussian profiles. In addition, we see that t_D increases approximately linearly as frequency decreases for the normal burst, and as frequency increases for the RS burst, with the former result similar to our recent simulations of normal bursts at lower frequencies [*Li et al.*, 2008b].

3.2. Source Beams and Langmuir Waves in Coordinate Space

[49] Figure 5 shows variations in tx-space of the Langmuir energy density W, beam speed v_b/c, beam width $\Delta v_b/c$, and beam number density N_b in the source region. Here $W = \int[\hbar\omega_L(k_L)N_L(t, x, k_L)]dk_L$, $v_b = (v_{\min} + v_{\max})/2$, $\Delta v_b = v_{\max} - v_{\min}$, $N_b = \int_{v_{\min}}^{v_{\max}} f_e(t, x, v)dv$, and $v_{\min}$ and $v_{\max}$ are the minimum and maximum speeds where $\partial f_e/\partial v \geq 0$, respectively. Note that the ion-sound waves are essentially thermal, because of weak ES decay and strong damping because $T_e/T_i = 1$, and so are not shown.

[50] We see from Figure 5a that after an impulsive, localized heating of the corona, due to the term S_b in (A16), L waves are quickly enhanced near the heating site and fill two "fans" in coordinate space. The rapid generation of L waves near the heating region is due mainly to the short heating duration δt, that makes it easy to preserve positive slopes in electron distribution functions, and to the large T_h in (A16) that produces fast electrons [*Benz*, 1993; *Bastian et al.*, 1998]. This is numerically demonstrated in our recent simulations [*Li et al.*, 2008b]. The fan shape of the Langmuir energy in tx-space occurs because of time-of-flight beam formation, quasilinear interaction between beam and L waves, and ES decay of the L waves, with dominance of the first two factors [*Li et al.*, 2002, 2003].

[51] Figure 5a shows that the fan associated with the upgoing beam is broader than that of the downgoing beam.

Further, the peak levels for the former persist over a wider range of coronal heights and last longer than for the latter. It is these features that lead to the longer duration of the normal burst than the RS burst at frequencies symmetric about f_{H0} in Figure 3b.

[52] The frequency difference between the onsets of nonthermal Langmuir waves driven by the upgoing and downgoing beams is $\delta f_L \approx 10$ MHz, which is smaller than the frequency separation $\delta f_H \approx 30$ MHz between the normal and RS bursts in Figure 4a. The reason for δf_H exceeding δf_L is that the beams must propagate larger distances from the heating site before the enhanced Langmuir waves reach the threshold for the nonlinear interaction in step iv in section 1 than before enhanced Langmuir waves are produced.

[53] Because Langmuir waves essentially trace the trajectory of the electron beam that drives them, and have negligible propagation speed compared with the beam speed, we can define a mean beam speed $\langle v_b \rangle$ such that it corresponds to a trajectory along the curve of maximal Langmuir energy density in tx-space [*Li et al.*, 2002]. Figure 5a shows that $\langle v_b \rangle \approx 0.18c$ for both beams. This indicates that the mean speeds of both beams remain nearly constant within the frequency range simulated, consistent with our recent simulations for normal metric type III bursts [*Li et al.*, 2008b].

[54] The mean beam speed $\langle v_b \rangle$ is different, by definition, from the average speed $\overline{v_b}$ used in (7) for predicting frequency drift rates, and also the speed v_b defined through the electron distribution function at the beginning of this section. The larger and smaller $\overline{v_b}$ than $\langle v_b \rangle$ for the normal and RS bursts, respectively, indicate that the values of $\langle v_b \rangle$, which is determined primarily by the beam-driven Langmuir waves [*Li et al.*, 2002, 2008b], can only describe semiquantitatively, not quantitatively, the drift rates of both bursts simulated. Nonetheless, for the normal burst simulated by *Li et al.* [2008b], $\langle v_b \rangle$ agrees quantitatively with $\overline{v_b}$. Further studies (not shown) find that, in general, $\overline{v_b}$ is different quantitatively from $\langle v_b \rangle$ (by a factor $\lesssim$30%), and $\overline{v_b}$ is more sensitive to variations in simulation parameters (e.g., T_e) than $\langle v_b \rangle$.

[55] Figure 5b shows that at two given coronal layers whose frequencies are symmetric about f_{H0}, the upgoing beam has much longer duration and higher speeds at the leading end than the downgoing beam, and the speeds at the trailing end for both beams are similar. Figure 5b shows that for the upgoing beam the speed v_b that corresponds to the trajectory of maximal Langmuir energy density in Figure 5a remains almost constant at 0.14 c, while for the downgoing beam the corresponding v_b reduces from 0.14 c to about 0.1 c as the beam moves toward the Sun (for $x \lesssim 0.8$ Gm). The difference in beam duration is shown, for instance, at $x \approx 0.18$ Gm (where $2f_p = 400$ MHz) the upgoing beam lasts about 0.85 s with $0.5\ c \lesssim v_b \lesssim 0.14\ c$, while the downgoing beam at $x \approx 0.097$ Gm (where $2f_p = 600$ MHz) lasts only about 0.3 s with $0.3\ c \lesssim v_b \lesssim 0.14\ c$. The longer duration of the upgoing beam occurs because the beams broaden because of velocity dispersion as they propagate, and the upgoing beam has traveled a greater distance from the heating site than the corresponding downgoing beam. However, we see that it is the beams with medium to low speeds ($v_b \lesssim 0.25\ c$) that are the dominant drivers for the significantly enhanced Langmuir waves in both regions away from the heating site in Figure 5a. Faster portions of the upgoing beam with $v_b \gtrsim 0.25\ c$ do not drive Langmuir waves effectively, since they are too weak (see Figure 5d).

[56] Figure 5c shows asymmetry in the spread Δv_b for the upgoing and downgoing beams. For instance, at $x \approx 0.18$ Gm, the upgoing beam quickly broadens after formation and reaches a peak $\Delta v_b/c \approx 0.13$, then narrows slowly. For the downgoing beam at $x \approx 0.097$ Gm, Δv_b increases gradually after the beam formation, reaches a peak $\Delta v_b/c \approx 0.05$ at $t \approx 0.4$ s, and then decreases slowly, but it usually much smaller than that of the upgoing beam. We see from Figure 5c that the locus of the peak Langmuir energy density in Figure 5a corresponds to $\Delta v_b/c \gtrsim 0.01$ for the upgoing beam, and for the downgoing beam to the same width for $x \gtrsim 0.8$ Gm but lower $\Delta v_b/c$ ($\sim$0.005, not shown in Figure 5c to avoid possible confusion with the adjacent 0.01 level) at smaller x. So the downgoing beam narrows in velocity space as it propagate toward the Sun.

[57] Figure 5d shows that the upgoing beam has larger number density than the downgoing beam. Therefore, as the downgoing beam propagates into dense corona, its relative number density N_b/n decreases more quickly than the upgoing beam that travels into the less dense corona, consistent qualitatively with the analysis of *Robinson and Benz* [2000]. The Langmuir growth rate ($\gamma_L \sim (\partial f/\partial v)/\omega_p$) is thus smaller for the downgoing beam. In addition, Figure 5d implies that both beams are rather weak. For example, $N_b/n \approx 2.4 \times 10^{-9}$ at $t \approx 1.0$ s and $x \approx 0.2$ Gm (where $n \approx 4.2 \times 10^{14}$ m^{-3}).

[58] The combined effects of smaller relative beam densities, narrower beam widths, and lower or equal beam speeds for the downgoing beam than the upgoing beam lead to weaker emission of Langmuir waves by the downgoing beam than by the upgoing beam. Consequently, the source radiation and subsequent remote radiation are asymmetric with respect to f_{H0} (and f_{F0}), as in section 3.1.

3.3. Phase Space Evolution of Source Beams and Waves

[59] We study here the evolution of the beam, and Langmuir and transverse waves in phase space within the source region.

3.3.1. Beam and Langmuir Waves

[60] Figure 6 shows the phase space electron distribution function $f_e(x, v)$ and the Langmuir wave occupation number $N_L(x, v)$ at two times, where v denotes both the electron speed and the Langmuir wave phase speed parallel to the beam velocity. Figure 6a shows that at $t_a = 0.4$ s the upgoing beam is within the region $x \approx (0.13-0.20)$ Gm, and the downgoing beam is at $x \approx (0.07-0.13)$ Gm. The two beams appear almost symmetric about x_0. We see that both beams have relaxed fully at low speeds between about 0.1 c and 0.2 c at $x \approx (0.14-0.15)$ Gm and $x \approx (0.11-0.12)$ Gm, respectively, as indicated by the vertical contour lines in Figure 6a.

[61] Figure 6b shows that the beam-driven L_0 waves are enhanced for $0.14 \lesssim x \lesssim 0.17$ Gm for the upgoing beam, and $0.09 \lesssim x \lesssim 0.12$ Gm for the downgoing beam, and peak at phase speeds $\sim 0.15c$ for the former and $\sim -0.15c$ for the latter. In addition, the L_0 waves are strongest for $x \approx (0.14-0.15)$ Gm and $x \approx (0.11-0.12)$ Gm, as expected from the flattening of the beams in these regions in Figure 6a.

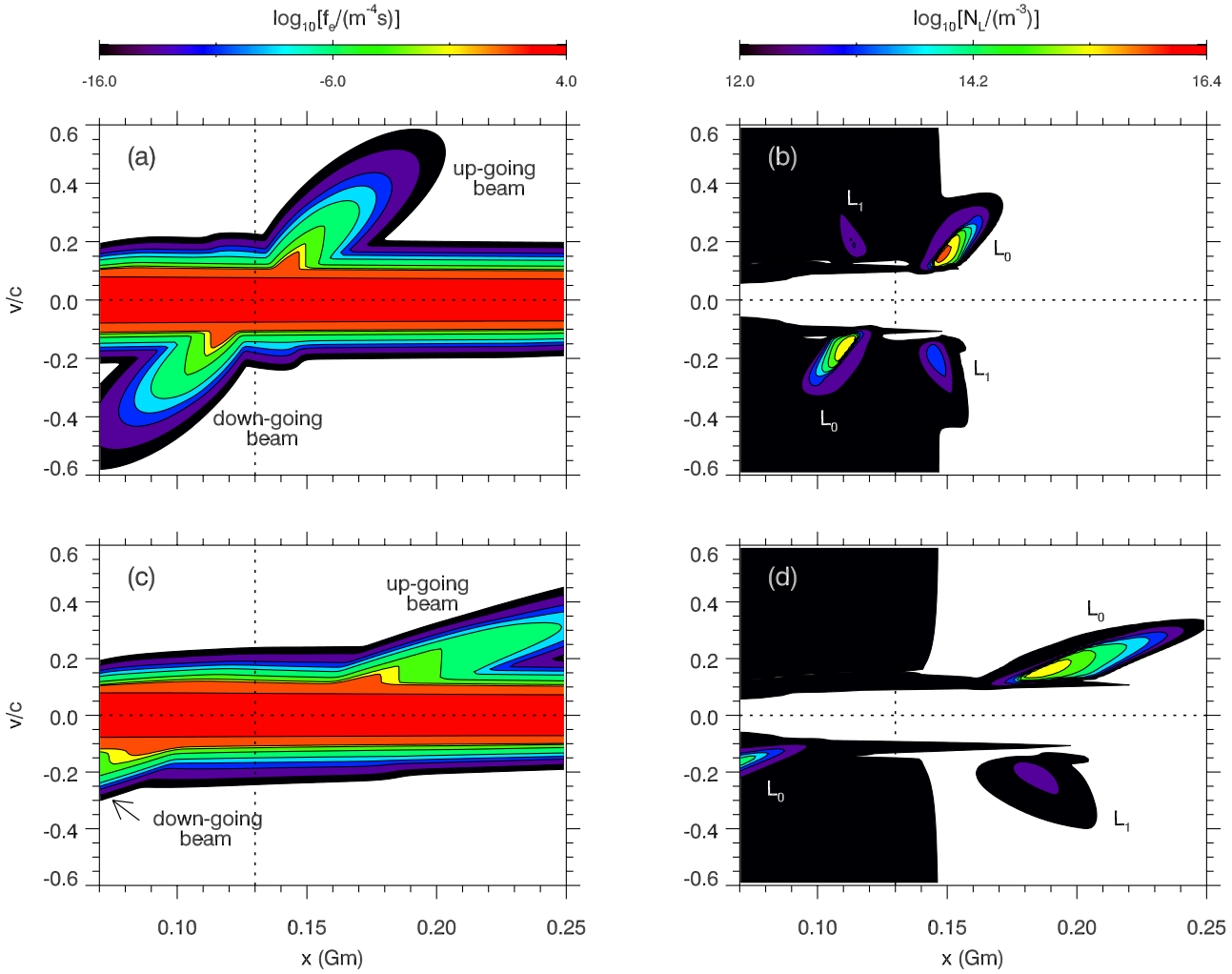

Figure 6. Phase space distributions of (a and c) electrons and (b and d) Langmuir waves at two times: t_a = 0.4 s (Figures 6a and 6b) and t_b = 1.2 s (Figures 6c and 6d). Dotted lines show the central heating location x_0 and speed or phase speed $v = 0$. In Figures 6b and 6d, the label L_0 stands for Langmuir waves driven by the beams, and L_1 stands for Langmuir waves produced by ES decay of the L_0 waves.

However, for $0.17 \lesssim x \lesssim 0.20$ Gm and $0.07 \lesssim x \lesssim 0.9$ Gm, the L waves are near thermal at this time, because the beams there are too weak to effectively drive L waves. The weakly enhanced Langmuir waves at $0.11 \lesssim x \lesssim 0.15$ Gm for $0.1 \lesssim |v/c| \lesssim 0.15$ are thermal Langmuir waves corresponding to the temperature T_h, due to the impulsive heating of the beams given by (A16) [*Li et al.*, 2002].

[62] Figure 6b also shows that the L_1 waves produced by the ES decay $L_0 \rightarrow L_1 + S_\theta$ have wave vectors opposite to the directions of propagation of the beams and are much weaker than the L_0 waves. We see from Figure 6b that the L_1 waves due to the downgoing beam are weaker than those associated with the upgoing beam.

[63] Figure 6c shows that at the later time t_b = 1.2 s the upgoing beam has arrived at more distant locations than at t_a. In fact, high speed electrons of both the upgoing and downgoing beams have exited the simulation box (at both ends). We see that the upgoing beam with $0.1 \lesssim v/c \lesssim 0.25$ at $x \approx (0.18–0.20)$ Gm has relaxed and so has the downgoing beam at $x \approx 0.075$ Gm. Note that now the downgoing electrons at $x = 0.08$ Gm no longer show a beam (i.e., $\partial f_e/\partial v < 0$), while the upgoing electrons at the symmetric location $x = 0.018$ Gm about x_0 display a relaxed beam. The L_0 waves in Figure 6d are strongly enhanced by the upgoing beam at $x \gtrsim 0.16$ Gm for $0.1 \lesssim v/c \lesssim 0.35$, and are only weakly driven by the downgoing beam within a smaller region $x \lesssim 0.1$ Gm for lower phase speeds $0.1 \lesssim |v/c| \lesssim 0.25$. Figure 6d also shows that the L_1 waves associated with the upgoing beam are enhanced while those linked to the downgoing beam are negligible.

3.3.2. Second Harmonic Transverse Waves

[64] Figure 7 shows variations of the $2f_p$ emission rate $\Gamma_H(k_H, \chi)$ with wave number k_H and angle χ at two locations x_a = 0.097 Gm and x_b = 0.18 Gm, respectively, for the two times in Figure 6. We choose these two locations so that the values of $2f_p$ there (i.e., 600 MHz and 400 MHz, respectively) are symmetric about f_{H0}.

[65] Figure 7a shows that at t_a = 0.4 s, the emission rate at x_a corresponding to the downgoing beam has a dominant backward (sunward-directed) peak at $k_H \approx 10.95$ m^{-1} and $\chi \approx 135°$ (and an associated forward, or anti-sunward-directed, peak near $k_H \approx 11.02$ m^{-1} and $\chi \approx 45°$). This peak is

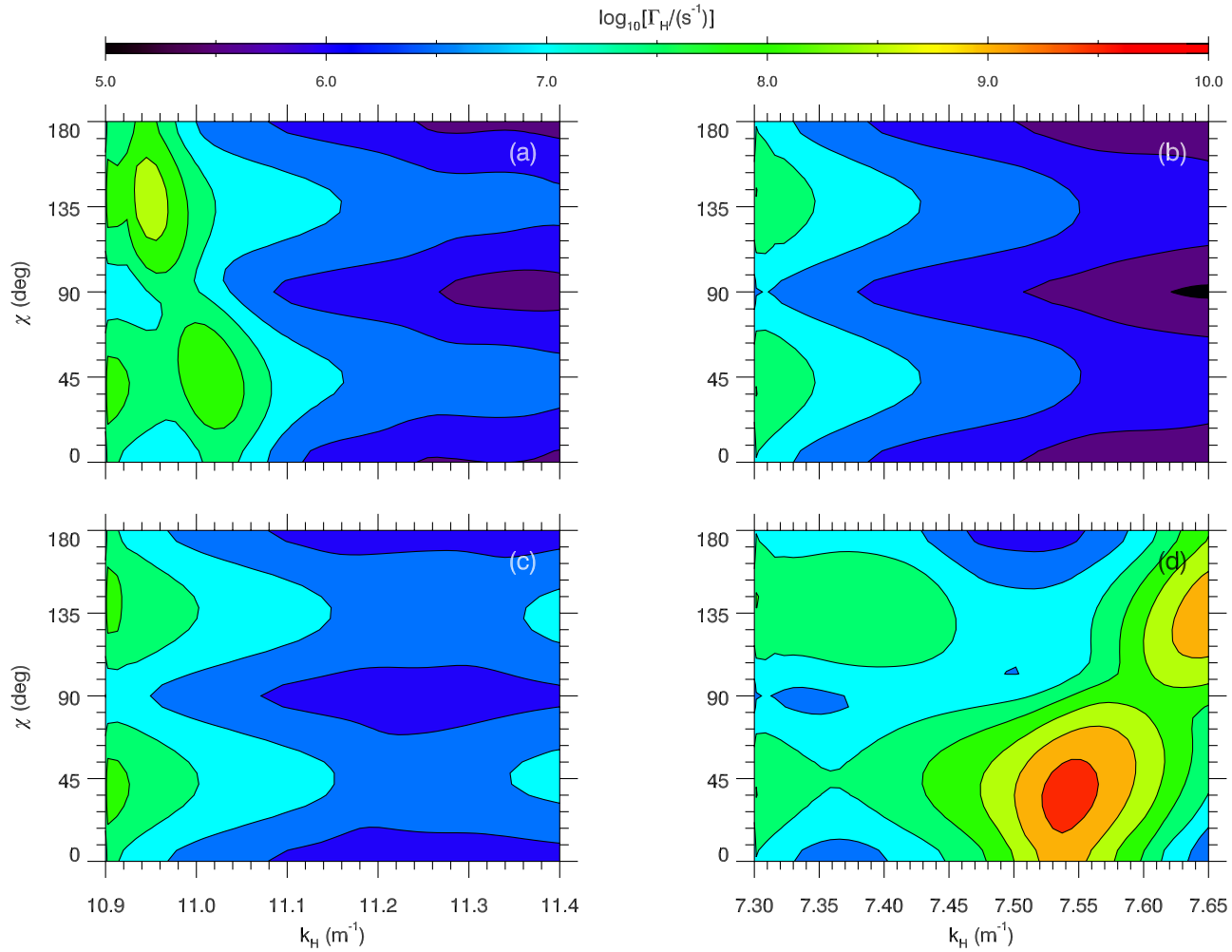

Figure 7. The $2f_p$ emission rate: (a and c) at source locations $x_a = 0.097$ Gm for the downgoing beam and (b and d) at $x_b = 0.18$ Gm for the upgoing beam, at the same times as in Figure 6: $t_a = 0.4$ s (Figures 7a and 7b) and $t_b = 1.2$ s (Figures 7c and 7d).

produced by the coalescence $L_0 + L_\theta \rightarrow H_1$, where the L_0 waves are driven by the downgoing beam, as shown in Figure 6b. Because of the stronger, backward-oriented L_0 waves than the L_θ waves here, the peak in Γ_H is oriented in the backward direction [*Li et al.*, 2005a]. In contrast, Figure 7b shows that at x_b, the emission rate is very low (near the thermal levels), and is symmetric about 90° with two peaks at 45° and 135°, respectively. The weak emission at x_b occurs since the Langmuir waves there are nearly thermal, in spite of the presence of a weak beam, as in Figures 6a and 6b. The near-quadrupolar radiation patterns in Figures 7a and 7b are consistent with previous analytical and numerical work [*Zheleznyakov and Zaitsev*, 1970; *Cairns*, 1987; *Willes et al.*, 1996; *Li et al.*, 2005a, 2008b].

[66] At the later time $t_b = 1.2$ s, Figure 7c shows that the emission rate at x_a is near thermal, because of the interaction $L_0 + L_\theta \rightarrow H_1$ between the weak L_0 waves and thermal Langmuir waves in Figure 6d. Figure 7d shows that at x_b the $2f_p$ emission rate is strongly enhanced, and has a forward peak near $k_H \approx 7.54$ m^{-1} and $\chi \approx 45°$ (and an associated backward peak near $k_H \approx 7.65$ m^{-1} and $\chi \approx 135°$). The strong emission at x_b occurs because of the coalescence $L_0 + L_1 \rightarrow H_1$ between the L_0 waves driven by the upgoing beam and associated L_1 waves in Figure 6d. Further, the dominance of the forward-oriented L_0 waves over the backward-oriented L_1 waves leads to the forward peak emission [*Li et al.*, 2005a]. Figure 7d also shows a slightly superthermal, backward-orientated peak at $k_H \approx 7.38$ m^{-1} and $\chi \approx 135°$, which is driven by the process $L_1 + L_\theta \rightarrow H_2$.

[67] Note that although the emission rates for both upgoing and downgoing beams are properly calculated here, contributions to the remote $2f_p$ radio flux are assumed to come only from the portion with $\chi \leq 90°$ (i.e., the anti-sunward hemisphere in wave vector space). Emissions at $\chi > 90°$ are neglected, since the observer is at Earth and the reflected $2f_p$ emission from the sunward-directed radiation is expected to be weak, as in our model in section 2. Further discussion of this assumption is given in section 5.

3.4. Effects of Langmuir Collisional Damping

[68] We study here the effects of Langmuir collisional damping on beam propagation, wave emissions in the source, and remote radiation, by setting $\gamma_c = 0$ in (A14) and comparing the corresponding results with those in sections 3.1 and 3.3. It is shown that collisional damping of Langmuir waves has major effects on the results and

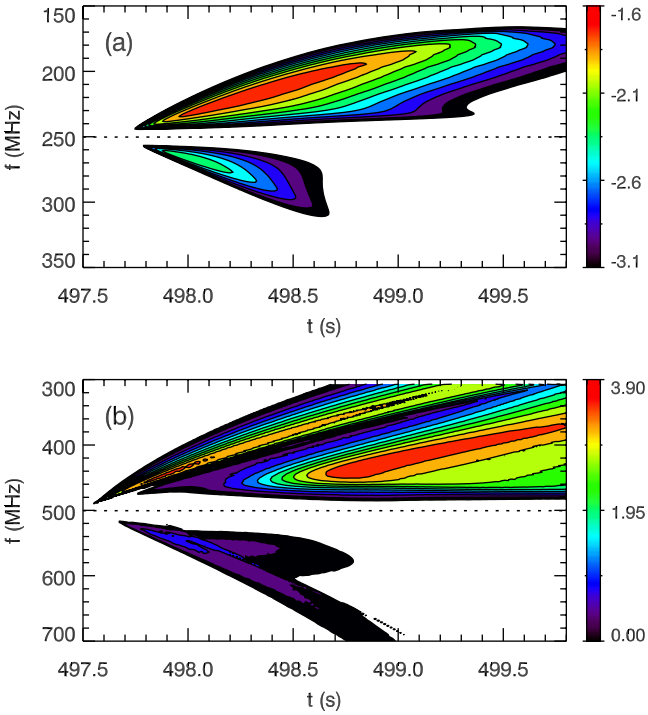

Figure 8. Predicted dynamic spectra at Earth for (a) f_p and (b) $2f_p$ radiation, in $\log_{10}[\mathcal{F}/(10^{-22}\ \mathrm{W\ m^{-2}\ Hz^{-1}})]$, when collisional damping of Langmuir waves is switched off and the other conditions are the same as in Figure 3. Note that the gray scales in Figures 8a and 8b are different from those in Figures 3a and 3b, respectively.

must be included. It significantly reduces the levels of Langmuir waves and thereby removes the secondary components of the radiation spectrum that would otherwise be predicted.

3.4.1. Dynamic Spectrum: Zero Langmuir Collisional Damping

[69] Figure 8 shows the dynamic spectra seen at Earth, when collisional damping of Langmuir waves is switched off and for otherwise identical parameters to Figure 3. Compared with Figures 3a and 3b, we see the following features:

[70] 1. The flux levels of both f_p and $2f_p$ emissions are higher, with the $2f_p$ flux about two orders of magnitude higher, but the f_p emission is still too weak to be observed.

[71] 2. The spectra show extra (fine) structures. For $2f_p$ emission with negative drift rates, there exists a secondary lane of stronger, longer-lasting emission than the first, primary lane, which corresponds to the normal burst in Figure 3b. The $2f_p$ emission with positive drift rates shows slow-drifting, extended-long tails, and the f_p emissions with either negative or positive drift rates display similar structures.

[72] 3. The onset times of both f_p and $2f_p$ emissions with either negative or positive drift rates are slightly earlier ($\lesssim$0.01 s) than in Figures 3a and 3b. The physics of these features is elaborated in the following paragraphs.

[73] The stronger remote radiation occurs since: First, the Langmuir energy levels are higher when collisional damping is switched off, as shown in detail in Figures 9b and 9d. Second, the source radiation is thus stronger than when collisional damping is included, because of stronger wave-wave interactions in steps ii–iv in section 1 [*Li et al.*, 2005a, 2005b]. Specifically, more successive EM decays and coalescences occur when collisional damping is not included, leading to higher levels of radiation being generated in the source region and thus propagating to the observer. In this case, the wave-wave processes are $L_i \rightarrow F_{i+1} + S_\theta$ for generation of f_p emission, and $L_j + L_{j+1} \rightarrow H_{j+1}$ and $L_i + L_\theta \rightarrow H_{i+1}$ for production of $2f_p$ emission, respectively, where $i = 0, 1, 2, j = 0, 1$, and the L_2 waves are the product of ES decay process $L_1 \rightarrow L_2 + S_\theta$. More details are given below when discussing the source emission in Figure 10.

[74] For $2f_p$ emission in Figure 8b, the first lane of the emission with negative drift rates is due mainly to the same emission processes to those in Figure 3b, except that now the levels of Langmuir waves are higher. Specifically, the emission is due to the processes $L_0 + L_1 \rightarrow H_1$, $L_0 + L_\theta \rightarrow H_1$, and $L_1 + L_\theta \rightarrow H_2$, with the first one dominant. The dominance of the beam-driven L_0 waves here leads to fast frequency drift of the radiation.

[75] The secondary lane of the $2f_p$ emission with negative drift rates is driven by processes associated with L_1 and L_2 waves: $L_1 + L_2 \rightarrow H_2$, $L_1 + L_\theta \rightarrow H_2$, and $L_2 + L_\theta \rightarrow H_3$, with the first one predominant (see more detailed discussions in sections 3.4.2 and 3.4.3). Since the L_1 and L_2 waves need sufficient time to develop to be above the nonlinear interaction thresholds [*Li et al.*, 2005a], there thus exist temporal gaps in Figure 8b between the first-lane and the second-lane emissions. In addition, since the L_1 waves have larger phase speeds than the L_0 waves (see Figure 9), the former are more weakly Landau-damped and live longer than the latter, even after the beam has passed and the L_0 waves have dropped back to thermal [*Li et al.*, 2003, 2008b]. It is the persistence of the L_1 waves that results in the long duration of the second-lane emission. The stronger emission in the second lane than the first lane occurs since the interaction $L_1 + L_2 \rightarrow H_2$ here is stronger than $L_0 + L_1 \rightarrow H_1$. Our previous work has shown that the resonant (L_1, L_2) pairs have smaller (absolute) wave numbers than the (L_0, L_1) pairs, which leads to relatively larger emission rates for the former pairs than the latter pairs [*Li et al.*, 2005a].

[76] The extended long tails in $2f_p$ emission with positive drift rates in Figure 8b and also f_p emission in Figure 8a occur because of coalescences and EM decays involving Langmuir waves produced by ES decays. Discussions similar to those in the previous paragraph apply to both $2f_p$ and f_p emissions here. For f_p emission, however, scattering smooths out the temporal features of the dynamic spectrum.

3.4.2. Phase Space Evolution of Beams and Langmuir Waves: Zero Langmuir Collisional Damping

[77] Figure 9 shows the phase space electron distribution function $f_e(x, v)$ and the Langmuir wave occupation number $N_L(x, v)$ when collisional damping on Langmuir waves is switched off and for otherwise identical parameters to Figure 6. We see from Figure 9a that at $t_a = 0.4$ s the primary features of the beam propagation are similar to those in Figure 6a. However, two secondary, weak, and slow ($0.15c \lesssim |v| \lesssim 0.3c$) beams show up near the heating site, in the velocity directions opposite to the two beams produced by the heating. These beams occur because

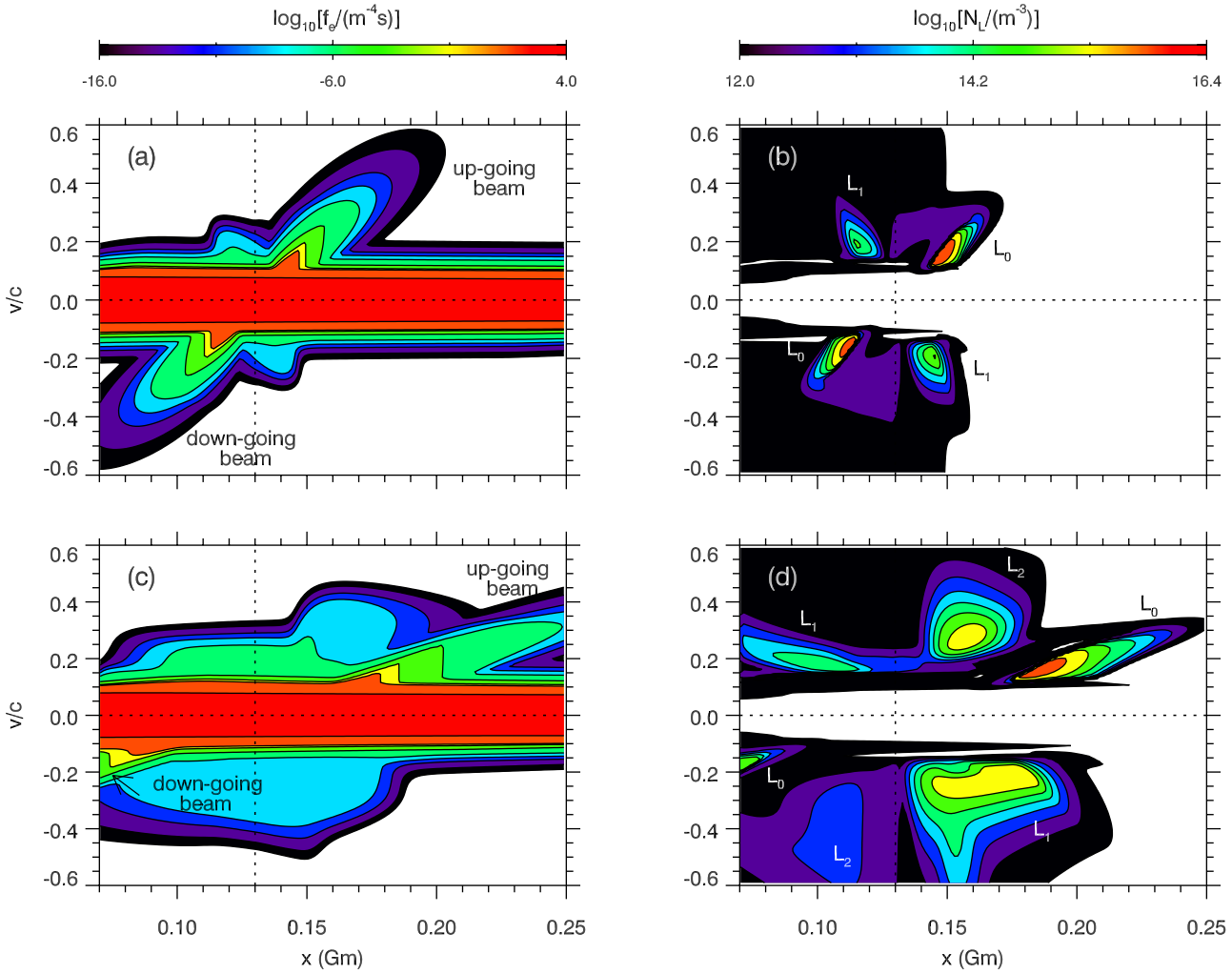

Figure 9. Phase space distributions of (a and c) electrons and (b and d) Langmuir waves at two times: t_a = 0.4 s (Figures 9a and 9b) and t_b = 1.2 s (Figures 9c and 9d), when collisional damping of Langmuir waves is switched off and the other conditions are the same as in Figure 6. In Figure 9d the label L_2 stands for Langmuir waves produced by ES decay of the L_1 waves.

thermal electrons absorb energy via quasilinear interactions from L_1 waves [*Ziebell et al.*, 2001; *Li et al.*, 2003], which are produced by ES decays of L_0 waves in the corresponding regions of Figure 9b.

[78] Figure 9b shows that both L_0 and L_1 waves, especially the latter, are stronger than in Figure 6b because of smaller losses when collisional damping is inoperative. The slightly enhanced Langmuir waves in the directions of beam propagation in and near the heating region are due to spontaneous emission from the heated electrons, as discussed in relation to Figure 6b in section 3.3.1. These thermal waves at large $|v|$ are now dissipated only by Landau damping and so last longer than when collisional damping is included [*Li et al.*, 2002]. Since the ES decay processes are slaved to the primary beam-Langmuir evolution [*Li et al.*, 2003], the propagation of the bidirectional beams in Figure 9a is similar to that in Figure 6a, in spite of the much stronger product Langmuir waves in Figure 9a.

[79] Figure 9c shows that at t_b = 1.2 s the propagation of the bidirectional beams remains similar to that in Figure 6c; however, the secondary beams now are more pronounced and spread out more in height than in Figure 9a. This occurs because the thermal electrons absorb more energy from the ES decay product Langmuir waves in Figure 9d, which are much stronger and expand over much broader heights than in Figure 9b and Figure 6d. In fact, now L_2 waves, which are the second-generation products of ES decay that propagate in the same direction as the beam-driven L_0 waves, are strongly enhanced by the process $L_1 \rightarrow L_2 + S_\theta$.

3.4.3. Phase Space Evolution of Second Harmonic Transverse Waves: Zero Langmuir Collisional Damping

[80] Figure 10 shows variations of the $2f_p$ emission rate with wave number and angle at x_a = 0.097 Gm and x_b = 0.18 Gm, respectively, when collisional damping of Langmuir waves is switched off and for otherwise identical parameters to Figure 7. We see from Figures 10a and 10b that at t_a = 0.4 s Γ_H for both the upgoing and downgoing beams is similar to Figures 7a and 7b, but slightly higher. Later, at t_b = 1.2 s, Figure 10c shows that radiation for the downgoing beam is significantly enhanced, with a forward-

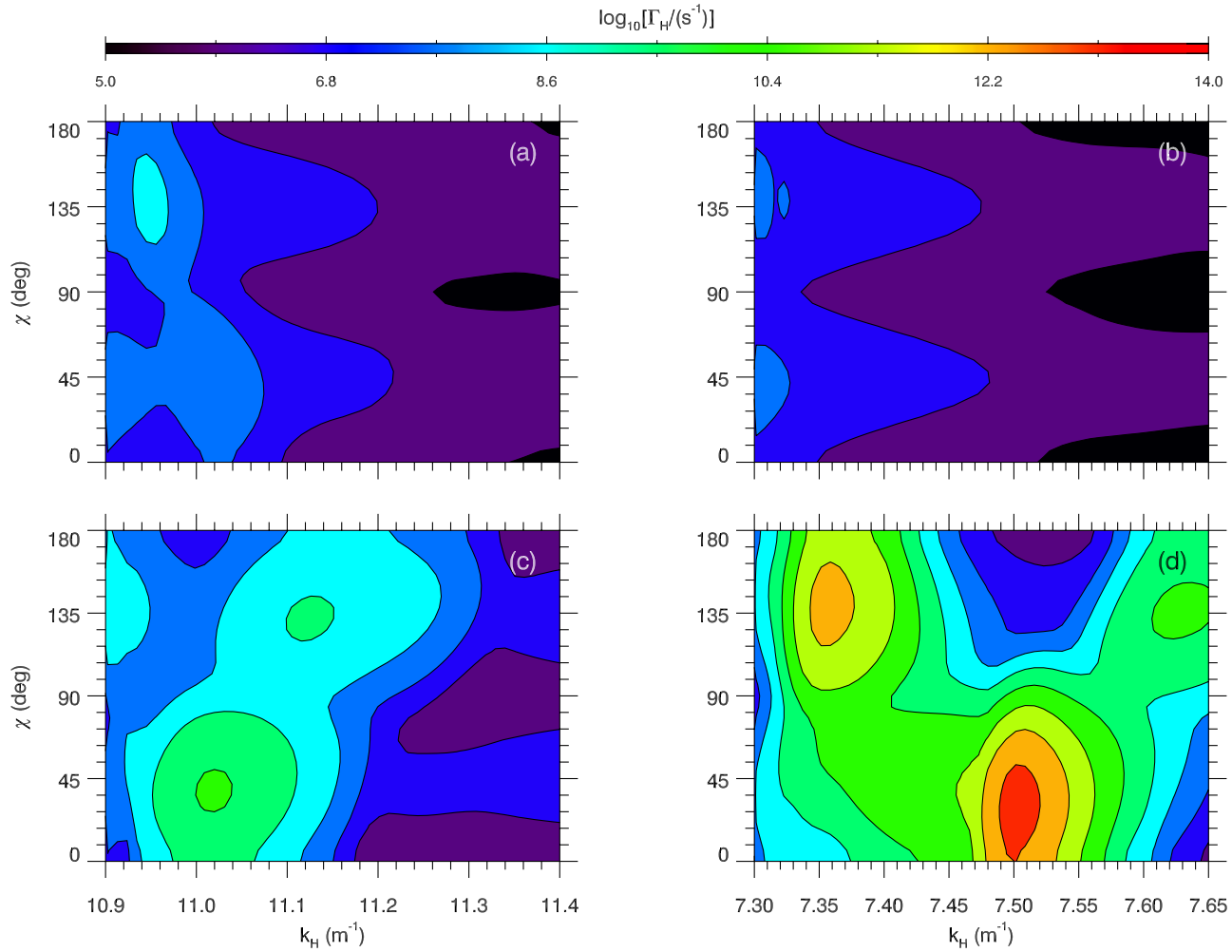

Figure 10. The $2f_p$ emission rate: (a and c) at source locations x_a = 0.097 Gm for the downgoing beam and (b and d) at x_b = 0.18 Gm for the upgoing beam, when collisional damping of Langmuir waves is switched off and the other conditions are the same as in Figure 7. Figures 10a and 10b, t_a = 0.4 s; Figures 10c and 10d, t_b = 1.2 s. Note that the gray scale here is different from that in Figure 7.

oriented peak with $\log_{10}[\Gamma_H/(s^{-1})] \approx 11.5$. This enhanced emission is primarily due to the interaction $L_1 + L_2 \rightarrow H_2$ between the strong L_1 and L_2 waves in Figure 9d. Figure 10d shows that for the upgoing beam the maximum emission rate is about 3 orders of magnitude higher than in Figure 7d, because of the much stronger coalescence $L_0 + L_1 \rightarrow H_1$ between the higher levels of L_0 and L_1 waves in Figure 9d than in Figure 6d. These enhanced nonthermal rates lead to the much more intense emission and new components in Figure 8.

4. Dependence of Results on Parameters

[81] The results in section 3 are for a specific set of beam acceleration and coronal parameters. Here we discuss the effects of varying these parameters.

[82] The effects of the heating parameters F_{acc} and T_h are similar. A decrease in F_{acc} (or T_h) leads to weaker beams and weaker and shorter-lasting radiation, consistent with theoretical predictions [*Robinson and Benz*, 2000]. Figure 11 shows the dynamic spectra seen at Earth for a lower heating fraction $F_{acc} = 2.5 \times 10^{-5}$ (a factor of 2 smaller) but otherwise identical parameters to Figure 3. We see that the flux levels of both f_p and $2f_p$ emissions are lower than in Figures 3a and 3b, respectively; e.g., the peak flux of the normal burst is reduced by a factor of 7. This occurs since the Langmuir energy densities (not shown) are lower than in Figure 5a because of fewer electrons being accelerated in this weaker heating event, and the source radiation is thus weaker because less Langmuir energy is available for conversion to EM radiation [*Li et al.*, 2002, 2005a, 2005b]. Further detailed studies of Figure 11 show that the average beam speed and the burst frequency drift rate are smaller, the maximum brightness temperature is lower, and the duration is shorter than in the nominal case. Figure 11b shows that, in addition, for $2f_p$ emission the peak flux of the RS burst is just above 10^{-22} W m^{-2} Hz^{-1}. Thus for an even weaker heating event, e.g., with F_{acc} further reduced (by, say, another factor of 2), only the normal burst is likely to be observed, since the RS burst is too weak (with peak flux about 4×10^{-23} W m^{-2} Hz^{-1}, not shown) for most instruments.

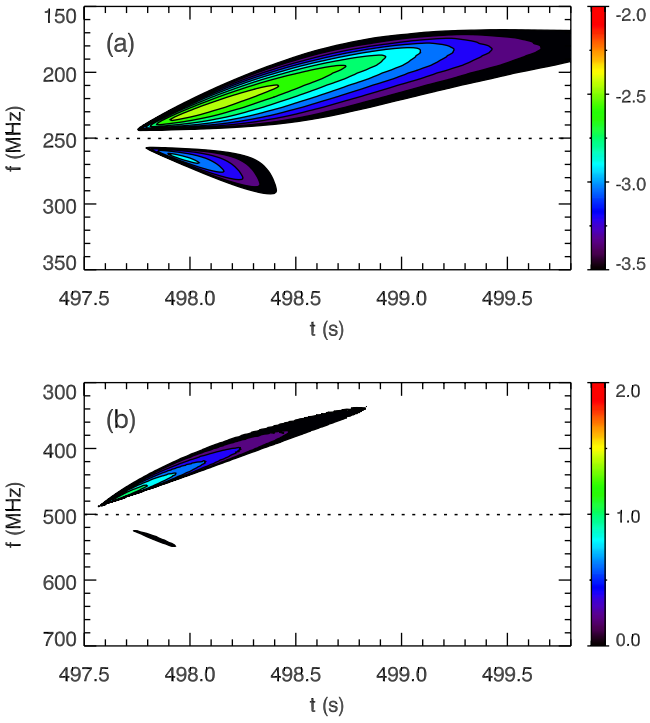

Figure 11. Predicted dynamic spectra at Earth for (a) f_p and (b) $2f_p$ radiation, in $\log_{10}[\mathcal{F}/(10^{-22}$ W m^{-2} Hz$^{-1})]$, for a lower acceleration fraction $F_{acc} = 2.5 \times 10^{-5}$ than in Figure 3 and otherwise identical parameters.

[83] Varying the spatial extent δx of the heating region (for $\delta x \lesssim 2 \times 10^{-3}$ Gm [*Aschwanden et al.*, 1995b; *Aschwanden*, 2002]) is found to have similar effects to varying F_{acc} and T_h; i.e., a smaller δx leads to weaker radiation. This occurs because the beam heating model (A16) produces fewer hot electrons for a smaller δx, and so the energy input to the type III system is less. However, we find that varying the heating duration δt ($\lesssim$3 ms [*Aschwanden et al.*, 1995b; *Aschwanden*, 2002]) has negligible effects. This occurs because our beam heating model (A16) is normalized with respect to δt.

[84] A change in the heating height x_0 causes a shift in the spectral frequency range, and changes in radio flux. For instance, when choosing $2f_p(x_0 = 0.0965$ Gm) = 600 MHz for otherwise identical parameters to the nominal case, the normal burst has twice the peak flux but the RS burst is briefer (lasting about 0.35 s from onset till termination). We find that heating the beams at even lower heights eventually leads to no significant radiation (i.e., flux below 10^{-22} W m^{-2} Hz^{-1}) associated with the downgoing beam, in agreement with previous theoretical predictions [*Robinson and Benz*, 2000].

[85] We find that increasing the electron temperature T_e has similar effects to those as decreasing F_{acc}; i.e., for a higher T_e radio emission is weaker, consistent with a theoretical model [*Robinson and Benz*, 2000]. For instance, when T_e = 3 MK, higher than in the nominal case, the observer only sees the normal burst, whose peak flux is lower by a factor of 5 than the corresponding burst for the nominal parameters. The decrease in radiation flux for an increase in T_e occurs mainly because the same set of heating parameters produces lower density beams when T_e is larger, and thus lower Langmuir levels although the collisional damping rate γ_c in (3) is slightly lower, and so weaker subsequent wave-wave interactions.

[86] Variations in the coronal ion temperature T_i leads to changes in radio flux at the observer. We find that an increase in T_i results in stronger radiation. For example, Figure 12 shows the dynamic spectra when T_i = 4 MK, twice as large as in the nominal case, for otherwise identical parameters to Figure 3. We see from Figure 12 that the normal burst is stronger, with a peak flux more than twice as big as the normal burst in Figure 3b, and the RS burst is slightly stronger than that in Figure 3b. The higher levels of radiation occurs because the ES decay rate increases for increasing T_i (or T_i/T_e), and thus the radiation rates increase [*Li et al.*, 2003, 2005a, 2005b].

[87] Varying the 3-D angular spread parameter β of the Langmuir and ion-sound spectra has significant effects on remote radiation. A smaller β (wider ES angular spectra in three dimensions) leads to lower radiation flux and shorter duration. For instance, when $\beta = 5$ (or characteristic angular spread $\Theta = 37°$), instead of the nominal value $\beta = 10$ (or $\Theta = 26°$) and otherwise identical parameters, the normal burst has a peak flux lower by a factor $\sim$3 and the RS burst survives only half as long (about 0.2 s from onset to termination). These changes in remote emission occur because of the following: First, for a lower β, the ES decay rate is lower, as shown in our previous work [*Li et al.*, 2005a, 2005b]. Second, the coalescence rates for H waves

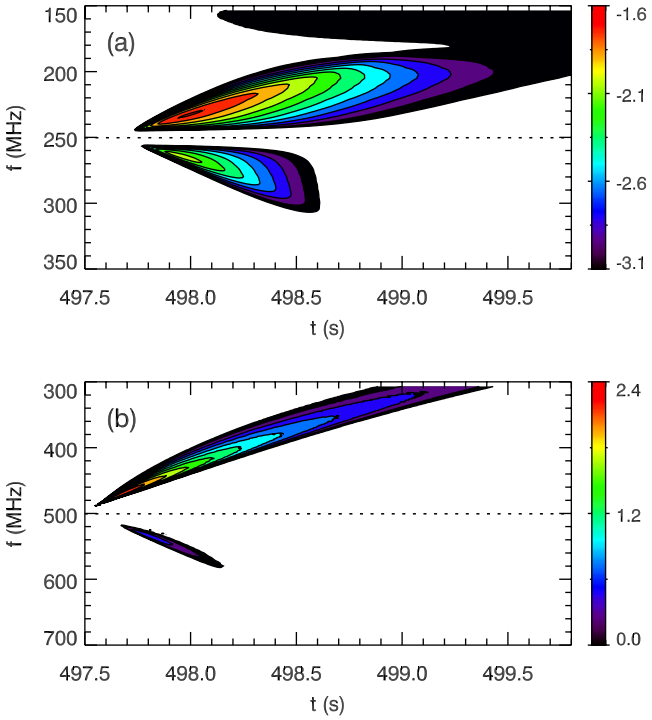

Figure 12. Predicted dynamic spectra at Earth for (a) f_p and (b) $2f_p$ radiation, in $\log_{10}[\mathcal{F}/(10^{-22}$ W m^{-2} Hz$^{-1})]$, for a higher ion temperature T_i = 4 MK than in Figure 3 and otherwise identical parameters. Note that the gray scales in Figures 12a and 12b are different from those in Figures 3a and 3b, respectively.

(and EM decay rates for F waves) in the source are thus lower [*Li et al.*, 2005a, 2005b], as is the remote radiation.

5. Discussion

[88] In general the simulation model yields results in quantitative or qualitative agreement with typical observations. Here we discuss the implications of the simulation results and limitations of the model for remote $2f_p$ radiation.

[89] We have found that the common frequency f_c, from which the paired bursts in Figure 4c appear to originate, is almost identical (with a 5 MHz difference) to the actual central frequency f_{H0} (i.e., 500 MHz) of the acceleration site. Since the actual central frequency and location of the acceleration site are inaccessible with current observations, the apparent intersection frequencies f_c of observed bidirectional bursts are inferred to be the central frequencies f_{H0} of the acceleration site [*Aschwanden et al.*, 1993, 1995b; *Meléndez et al.*, 1999; *Xie et al.*, 2000]. Our simulations thus support this assumption to a very high degree of accuracy, but predict that the true central frequency is about 1% higher.

[90] We have shown in section 4 that weak heating (small F_{acc} or/and T_h), and/or limited heating region (small δx), and/or high electron temperature T_e can lead to a weak or negligible RS burst, with only a normal burst likely observable. One implication of these results is that if only a normal burst is observed, not a pair of normal-RS bursts, the heating for the beams may still be bidirectional and symmetric but just be weaker, and/or the heating is more limited in spatial extent, and/or the corona has a higher electron temperature than for bidirectional radio events.

[91] The effect of varying β (or Θ) on bidirectional bursts shown here is only semiquantitative. This is because the 3-D ES wave angular spectra are parameterized via (A17) using the simulated 1-D ES wave spectra. Future work should explore this effect quantitatively, by simulating the ES wave angular spectra directly in three dimensions, or at least in a 2-D system that is symmetric about the beam direction, which was studied numerically very recently [*Ziebell et al.*, 2008].

[92] In our model we have neglected contributions to the $2f_p$ radiation observed remotely from the $2f_p$ emission that is sunward-directed in the source region, by assuming that the remote $2f_p$ emission originates solely from the initially anti-sunward-directed $2f_p$ emission. For the downgoing beam, source H waves in the anti-sunward direction dominate those in the sunward direction, while the situation is reversed for the upgoing beam, as shown in Figure 7. So by neglecting the contributions from the sunward-directed emission, the $2f_p$ flux at the observer is underestimated, especially for the RS burst. However, these sunward-directed H waves need to propagate further down toward the Sun until they are reflected back to the anti-sunward direction and eventually reach the remote observer. During the course of their propagation, scattering and free-free absorption will delay and damp these waves, probably by a large amount. Accordingly it is likely that a remote observer will detect much lower fluxes than would predicted from the source H waves with the assumption of no damping. It is plausible (but remains to be demonstrated) that the present results for $2f_p$ flux will remain basically unchanged, except for their temporal profile.

[93] Similarly to our recent work [*Li*, 2007; *Li et al.*, 2008b], the temporal evolution of the radio flux of normal and RS bursts (not shown) shows fast decay and slow rise after the emission onset, resembling the corresponding temporal variation of the Langmuir energy levels in the source (not shown) [cf. *Li et al.*, 2008b, Figure 8]. However, slow decay and fast rise is generally expected according to observations [e.g., *Aschwanden et al.*, 1993; *Xie et al.*, 2000]. Previous simulations [*Jaeger and Westfold*, 1950; *Riddle*, 1974] have shown that the sunward-directed $2f_p$ emission can be reflected back and reach the observer at later times than the anti-sunward-directed $2f_p$ emission, and lead to an approximately exponential tail with low flux levels. So the reason for the difference in the temporal profiles of the $2f_p$ flux between the predicted and observed may be due to the neglect of the sunward-directed $2f_p$ emission in the source. In addition, the difference can be caused by other effects, such as trapping of Langmuir waves by density fluctuations, as discussed previously [*Li et al.*, 2008b].

6. Conclusions

[94] We have presented the first simulations of bidirectional type III bursts seen by a remote observer, using an extended version of our original simulation model and also realistic beam acceleration and coronal parameters. These simulations are based on quasilinear equations augmented with terms for Langmuir ES decay, and on nonlinear wave-wave processes leading to emissions of EM waves. The model includes the structure of the 3-D source region, dynamics of the beam and waves within the source, and radiation propagation from the source to the observer. In the extended model we have incorporated more realistic 3-D source structure by including an increase in the source size with source height, and have included the effects of collisional damping on Langmuir waves. The simulated dynamic spectrum for an observer at Earth agrees semiquantitatively with observations.

[95] The simulated dynamic spectra of both the RS and normal bursts observed at Earth for representative parameters are studied in detail in association with the dynamics of the beams and waves in the source. The spectral characteristics predicted by the simulations for RS and normal bursts, including the radiation flux, brightness temperature, frequency drift rate, and duration, are compared with typical observations. The main results are as follows:

[96] 1. The flux levels of $2f_p$ emission are much greater than those of f_p emission, which is unlikely to be observable for typical radio instruments. This occurs mainly because of the much stronger free-free absorption of f_p emission than of $2f_p$ emission, the weaker generation of f_p emission in the source region, and the additional scattering-induced damping of f_p radiation for the given simulation conditions. Consequently, the $2f_p$ emission is dominant, consistent with observations and previous theoretical predictions [*Robinson and Benz*, 2000].

[97] 2. The normal and RS bursts show an up-down asymmetry. The normal burst has higher flux levels and brightness temperature, and lasts longer than the RS burst, consistent with observations. This occurs because the downgoing beam is weaker, not faster, and narrower in velocity

space than the upgoing beam, and the RS burst experiences stronger free-free absorption than the normal burst, in agreement with theoretical predictions.

[98] 3. The flux levels, and the trends of variations with frequency of the simulated fluxes of the normal and RS bursts are consistent with observations.

[99] 4. The frequency drift rates of both normal and RS bursts are consistent with observations, and agree semiquantitatively with the relation (7) between frequency drift rate and beam speed for the simulated beam dynamics and the assumed density model.

[100] 5. Collisional damping of Langmuir waves reduces the levels of Langmuir waves and thus quenches the series of ES decays faster than when damping by collisions is excluded. Consequently, successive radiation interactions are weaker, which result in lower flux levels and less structured radio emission profiles. Collisional damping of Langmuir waves must be included for coronal type III bursts at the high frequency range (300 MHz to 700 MHz) studied.

[101] The effects of varying coronal and beam acceleration parameters have been studied and illustrated. First, we find that weaker heating or higher coronal electron temperature can lead to the presence of only a normal burst, with a RS burst that is too weak to be observable. Second, when the acceleration site is low enough, we predict also that only the normal burst is observable. Both effects are consistent with theoretical analysis [*Robinson and Benz*, 2000]. Third, when the coronal ion temperature increases, the simulated f_p and $2f_p$ radio fluxes are higher, yet the f_p emission remains unobservable. Finally, for wider 3-D Langmuir and ion-sound angular spectra, the radiation is weaker and lasts shorter.

[102] Future work should model the propagation of $2f_p$ emission better, especially for $2f_p$ radiation that is sunward-directed in the source. This requires better modeling of its reflection and scattering. In addition, in the future we will explore directly the effects of 3-D beam propagation and completely 3-D modeling of the Langmuir and ion-sound wave processes on the radiation source, and subsequently on the dynamic spectra of bidirectional type III bursts. Furthermore, the effects of stochastic wave growth [*Robinson*, 1992; *Robinson et al.*, 1992, 1993; *Robinson and Cairns*, 1993] on remote radiation will be incorporated, via evolution of the beam-Langmuir system amid ambient density fluctuations [*Li et al.*, 2006c].

Appendix A: Simulation Model for the Propagation and Production of Radiation

[103] We assume that rays with different wave numbers k_{Ts} and polar angles χ_s are generated at a location x_s within the 1-D simulation box in Figure 1 over a very short period $(t_s, t_s + t_\varepsilon)$ and propagate as a bundle at the average group speed $\langle v_T(x; x_s)\rangle$ from x_s to d, taking into account refraction and reflection effects [*Li et al.*, 2006b]. The number density of photons at frequency f_s due to source radiation at x_s with emission rate Γ_T is [*Li*, 2007]

$$n_T(t_s,x_s,f_s) = \frac{t_\epsilon}{4\pi^2}\int dk_{Ts}\int_0^{\chi_T} d\chi_s \times \left[k_{Ts}^2 \sin\chi_s\ \Gamma_T(t_s,x_s,f_s,k_{Ts},\chi_s)\right]. \quad \text{(A1)}$$

Here $T = F$ or H, $\chi_F = 2\pi$, $\chi_H = \pi$, and Γ_F and Γ_H are the nonlinear rates for the radiation processes in steps iii and iv in section 1, which are given by *Li et al.* [2005a, 2005b]. Here f_s is given via the dispersion relation $\omega_T^2(x, k_T) = \omega_p^2(x) + k_T^2c^2$, so $f_s \approx f_p(x_s)$ for f_p emission, and $f_s \approx 2\,f_p(x_s)$ for $2f_p$ emission.

[104] Including the 3-D source character, scattering, and free-free absorption effects semiquantitatively, the change in photon number density at the observer at time t, due to the source layer at (t_s, x_s, f_s) is [*Li et al.*, 2008a]

$$\mathcal{N}_T(t,r,f;t_s,x_s,f_s) = g_T \exp\left[-\frac{(t'_T - t_T)}{t_d}\right]\exp(-\tau_T) \times \left\{\frac{\Omega_b(R_\odot + d)^2}{\Omega_T r^2} n_T(t_s,x_s,f_s)\right\}, \quad \text{(A2)}$$

where

$$g_F = \eta_F\,\Delta t/t_d, \quad \text{(A3)}$$

$$g_H = 1, \quad \text{(A4)}$$

$$t = t'_T + t_p, \quad \text{(A5)}$$

$$t'_F \geq t_F, \quad \text{(A6)}$$

$$t'_H = t_H, \quad \text{(A7)}$$

$$t_T = \int_{x_s}^{d} \frac{dx}{\langle v_T(x;x_s)\rangle}, \quad \text{(A8)}$$

$$t_p = (r - R_\odot - d)/c, \quad \text{(A9)}$$

$$f = f_s. \quad \text{(A10)}$$

In (A2), the term inside the curly brackets describes conservation of photons generated by the finite 3-D source layer in the absence of scattering and free-free absorption effects, while the first two factors and the third factor include these scattering and absorption effects, respectively. The quantity η_F in (A3) describes the fraction of f_p emission in the source region that can escape to infinity, provided there are no other loss mechanisms, and is given by equation (33) of *Li et al.* [2008a]. The speeds $\langle v_T(x; x_s)\rangle$ in (A8) are given by equations (2) and (3) of *Li et al.* [2008a] for f_p and $2f_p$ emission, respectively, based on tracing representative rays in three dimensions [*Li et al.*, 2006b]. Because of scattering f_p emission is time delayed following the assumption 4 in section 2, while time delay for $2f_p$ emission is negligible. Here t_d is a time constant due to scattering of f_p emission and is given by equation (38) of *Li et al.* [2008a] by solving the Fokker-Planck equation, and

Δt is the time resolution of the observing instrument (that is assumed to be same as the time resolution of the simulations). Free-free absorption is described via the optical depth τ_T. The relation (A10) indicates that the frequency of radiation is unchanged during propagation. Thus in deriving (A2) the effects of refraction, reflection, free-free absorption, and scattering are treated approximately, in a way that effectively includes the average solutions to a radiative transfer equation, except for the scattering of $2f_p$ emission.

[105] The radio flux measured by the observer due to radiation from the above source layer is

$$\mathcal{F}_T(t,r,f;t_s,x_s,f_s) = \frac{\hbar\omega_{Ts}c}{2\Delta f}\mathcal{N}_T(t,r,f;t_s,x_s,f_s), \tag{A11}$$

where $\mathcal{N}_T$ is given by (A2). Here $\omega_{Ts} = 2\pi f_s$, and Δf is the frequency resolution of the instrument, which is assumed to be same as the frequency resolution of the simulations. The factor of one half appears in (A11) because only electric (not total) energy is measured.

[106] The dynamic spectrum $\mathcal{S}_T$ seen by the observer is obtained by summing (A11) over t_s and x_s:

$$\mathcal{S}_T(t,r,f) = \sum_{t_s=0}^{t_M}\sum_{x_s=d-l}^{d}\mathcal{F}_T(t,r,f;t_s,x_s,f_s), \tag{A12}$$

where t_M is the duration of simulations.

[107] To evaluate the radiation emission rates Γ_F and Γ_H used in (A1) we need to solve for the dynamic evolution of beam, Langmuir waves, and ion-sound waves. This is achieved by solving the following generalized quasilinear equations in one dimension for distribution functions $f_e(t, x, v)$, $N_L(t, x, k_L)$, and $N_S(t, x, k_S)$ of electrons, Langmuir waves, and ion-sound waves, respectively [*Li et al.*, 2005a, 2006b], as assumed in point 2 in section 2

$$\frac{\partial f_e(t,x,v)}{\partial t} + v\frac{\partial f_e(t,x,v)}{\partial x} = \frac{\partial}{\partial v}[A_L f_e(t,x,v)] + \frac{\partial}{\partial v}\left[D_L\frac{\partial f_e(t,x,v)}{\partial v}\right] + S_b, \tag{A13}$$

$$\frac{\partial N_L(t,x,k_L)}{\partial t} + v_L\frac{\partial N_L(t,x,k_L)}{\partial x} - \frac{\partial\omega_L}{\partial x}\frac{\partial N_L(t,x,k_L)}{\partial k_L} = \alpha_L + \gamma_L N_L(t,x,k_L) - \gamma_c N_L(t,x,k_L) + \Gamma_L, \tag{A14}$$

$$\frac{\partial N_S(t,x,k_S)}{\partial t} + v_S\frac{\partial N_S(t,x,k_S)}{\partial x} = \alpha_S + \gamma_S N_S(t,x,k_S) + \Gamma_S. \tag{A15}$$

Here t, x, v, and k_L and k_S stand for time, position, speed, and wave numbers, respectively.

[108] The nonlinear rates Γ_L and Γ_S in (A14) and (A15) are the projections into the x-direction of the corresponding 3-D rates for the process in step ii in section 1 [*Li et al.*, 2005a]. The wave numbers k_L and k_S are given via the resonance condition $\omega_L = k_L v$ and the dispersion relations $\omega_L^2 = \omega_p^2 + 3k_L^2 v_e^2$ and $\omega_S = k_S v_S$. Here $\omega_p = (ne^2/m\varepsilon_0)^{1/2}$, $v_e = (k_B T_e/m)^{1/2}$, and m, and e, T_e are the electron mass, and charge, respectively, $v_L = \partial\omega_L/\partial k_L$ is the Langmuir group speed, $v_S = [(1 + 3T_i/T_e)k_B T_e/m_i]^{1/2}$ is the ion sound speed, and m_i is the ion mass. The coefficients A_L, α_L, α_S, and D_L, γ_L, and γ_S describe spontaneous and induced emission, respectively [*Li et al.*, 2002]. The quantity γ_c in (A14) is the damping rate of Langmuir waves due to electron-ion collisions and is given by (4). Similar quasilinear equations were numerically solved in earlier work [e.g., *Takakura and Shibahashi*, 1976; *Magelssen and Smith*, 1977; *Grognard*, 1985; *Ziebell et al.*, 2001; *Kontar and Pecseli*, 2002; *Li et al.*, 2003]. However, this is the first time that these equations are solved to obtain the dynamic spectrum of bidirectional type III bursts observed remotely.

[109] The term S_b in (A13) describes the acceleration of electrons during flares [*Robinson and Benz*, 2000; *Li et al.*, 2002], with

$$S_b = \frac{F_{acc}}{\sqrt{\pi}\,\delta t}[f_h(v,T_h) - f_c(v,T_e)] \times \exp\left[-\frac{(t-t_0)^2}{(\delta t)^2} - \frac{(x-x_0)^2}{(\delta x)^2}\right]. \tag{A16}$$

It represents a specific heating of a fraction F_{acc} of electrons from T_e to T_h ($>T_e$) over a typical region (δt, δx) centered at (t_0, x_0), which leads to formation of a beam via time-of-flight effects. We assume f_h and f_c are Maxwellian, following previous work [e.g., *Magelssen and Smith*, 1977; *Grognard*, 1985].

[110] The 1-D ES wave spectra in (A14) and (A15) are used to construct the corresponding 3-D spectra, using the method developed by *Li et al.* [2005a, 2005b]. These 3-D spectra are then used directly to calculate the EM emission rates Γ_F and Γ_H, as assumed in point 2 in section 2. The 3-D spectra N_M^{3D} ($M = L$ or S) are assumed to be axisymmetric along the direction of beam propagation and have arc-shaped angular forms [*Willes et al.*, 1996; *Li et al.*, 2005a]

$$N_M^{3D}(\mathbf{k}_M) = \mathcal{N}_M^{3D}(k_M)\ \exp(\beta\ \cos\theta_M). \tag{A17}$$

Here $\theta_M = \tan^{-1}(k_{M\rho}/k_{Mx})$ is the angle between the wave vector $\mathbf{k}_M$ and the x-direction, and k_{Mx} and $k_M\rho$ are the parallel and perpendicular wave numbers, respectively. The quantity $\mathcal{N}_M^{3D}(k_M)$ is related to $N_M(k_M)$ given by (A14) and (A15), via equation (41) of *Li et al.* [2005a]. The characteristic angular range of the arc spectrum is $\Theta \approx \cos^{-1}[(\beta - 1)/\beta]$, where β is a positive parameter, and a wide angular range corresponds to small β. Arc spectra are good approximations for the L and S wave spectra obtained via numerical solutions of the Zakharov equations, where the evolution of beam-driven Langmuir waves through weak turbulence ES decay toward strong turbulence effects was studied [*Robinson and Newman*, 1989]. Arc spectra are also qualitatively consistent with the 2-D L and S wave spectra obtained in recent simulations of the dynamics of beam-plasma system including quasilinear interactions and Langmuir ES decay process [*Ziebell et al.*, 2008].

[111] **Acknowledgments.** The Australian Research Council supported this work.

[112] Amitava Bhattacharjee thanks the reviewers for their assistance in evaluating this paper.

References

Allen, C. W. (1947), Interpretation of electron densities from corona brightness, *Mon. Not. R. Astron. Soc.*, *107*, 426.

Alvarez, H., and F. T. Haddock (1973), Solar wind density model from km-Wave type III bursts, *Sol. Phys.*, *29*, 197.

Aschwanden, M. J. (2002), Particle acceleration and kinematics in solar flares — A synthesis of recent observations and theoretical concepts, *Space Sci. Rev.*, *101*, 1.

Aschwanden, M. J., A. O. Benz, and R. A. Schwartz (1993), The timing of electron beam signatures in hard X-ray and radio: solar flare observations by BATSE/Compton Gamma-Ray Observatory and PHOENIX, *Astrophys. J.*, *417*, 790.

Aschwanden, M. J., R. A. Schwartz, and D. M. Alt (1995a), Electron time-of-flight differences in solar flares, *Astrophys. J.*, *447*, 923.

Aschwanden, M. J., A. O. Benz, B. R. Dennis, and R. A. Schwartz (1995b), Solar electron beams detected in hard X-rays and radio waves, *Astrophys. J.*, *455*, 347.

Bastian, T. S. (2004), Low-frequency solar radiophysics with LOFAR and FASR, *Planet. Space Sci.*, *52*, 1381.

Bastian, T. S., A. O. Benz, and D. E. Gary (1998), Radio emission from solar flares, *Annu. Rev. Astron. Astrophys.*, *36*, 131.

Baumbach, S. (1937), Strahlung, ergiebigkeit und elektronendichte der sonnenkorona, *Astron. Nachr.*, *263*, 131.

Benz, A. O. (1993), *Plasma Astrophysics*, Kluwer Acad., Dordrecht, Netherlands.

Benz, A. O., C. H. Barrow, B. R. Dennis, M. Pick, A. Raoult, and G. Simnett (1983), X-ray and radio emissions in the early stages of solar flares, *Sol. Phys.*, *83*, 267.

Cairns, I. H. (1987), Second harmonic plasma emission involving ion sound waves, *J. Plasma Phys.*, *38*, 179.

Cairns, I. H. (2000), Role of collective effects in dominance of scattering off thermal ions over Langmuir wave decay: Analysis, simulations, and space applications, *Phys. Plasmas*, *7*, 4901.

Cairns, I. H. (2004), Solar, interplanetary, planetary, and related extra-solar system science for LOFAR, *Planet. Space Sci.*, *52*, 1423.

Dulk, G. A. (2000), Type III solar radio bursts at long wavelengths, in *Radio Astronomy at Long Wavelengths*, *Geophys. Monogr. Ser.*, vol. 119, edited by R. G. Stone et al., p. 115, AGU, Washington, D. C.

Ginzburg, V. L. (1964), *The Properties of Electromagnetic Waves in Plasma*, Pergamon, New York.

Grognard, R. J. M. (1985), Propagation of electron streams, in *Solar Radiophysics*, edited by D. J. McLean and N. R. Labrum, p. 253, Cambridge Univ. Press, Cambridge, U. K.

Hughes, M. P., and R. L. Harkness (1963), Spectral observations of solar radio bursts. IV. The exciters of fast-drift bursts, *Astrophys. J.*, *138*, 239.

Jaeger, J. C., and K. C. Westfold (1950), Equivalent path and absorption for electromagnetic radiation in the solar corona, *Aust. J. Sci. Res. A*, *3*, 376.

Klassen, A., M. Karlicky, and G. Mann (2003), Superluminal apparent velocities of relativistic electron beams in the solar corona, *Astron. Astrophys.*, *410*, 307.

Klein, K.-L., S. Krucker, G. Trotter, and S. Hoang (2005), Coronal phenomena at the release of solar energetic electron events, *Astron. Astrophys.*, *431*, 1047.

Kontar, E. P., and H. L. Pecseli (2002), Nonlinear development of electron-beam-driven weak turbulence in an inhomogeneous plasma, *Phys. Rev. E*, *65*, 066408, doi:10.1103/PhysRevE.65.066408.

Leblanc, Y., G. A. Dulk, I. H. Cairns, and J.-L. Bougeret (2000), Type II flare continuum in the corona and solar wind, *J. Geophys. Res.*, *105*, 18,215.

Li, B. (2007), Simulated dynamic spectra: A group of coronal type III bursts, *Astrophys. J.*, *666*, L129.

Li, B., P. A. Robinson, and I. H. Cairns (2002), Multiple electron beam propagation and Langmuir wave generation in plasmas, *Phys. Plasmas*, *9*, 2976.

Li, B., A. J. Willes, P. A. Robinson, and I. H. Cairns (2003), Dynamics of beam driven Langmuir and ion-acoustic waves including electrostatic decay, *Phys. Plasmas*, *10*, 2748.

Li, B., A. J. Willes, P. A. Robinson, and I. H. Cairns (2005a), Second harmonic electromagnetic emission via beam-driven Langmuir waves, *Phys. Plasmas*, *12*, 012103, doi:10.1063/1.1812274.

Li, B., A. J. Willes, P. A. Robinson, and I. H. Cairns (2005b), Dynamics of fundamental electromagnetic emission via beam-driven Langmuir waves, *Phys. Plasmas*, *12*, 052324, doi:10.1063/1.1906214.

Li, B., P. A. Robinson, and I. H. Cairns (2006a), Numerical simulations of type III solar radio bursts, *Phys. Rev. Lett.*, *96*, 145005, doi:10.1103/PhysRevLett.96.145005.

Li, B., P. A. Robinson, and I. H. Cairns (2006b), Numerical modeling of type III solar radio bursts in the inhomogeneous solar corona and interplanetary medium, *Phys. Plasmas*, *13*, 092902, doi:10.1063/1.2355660.

Li, B., P. A. Robinson, and I. H. Cairns (2006c), Quasilinear calculation of Langmuir wave generation and beam propagation in the presence of density fluctuations, *Phys. Plasmas*, *13*, 082305, doi:10.1063/1.2218331.

Li, B., I. H. Cairns, and P. A. Robinson (2008a), Simulations of coronal type III solar radio bursts: 1. Simulation model, *J. Geophys. Res.*, *113*, A06104, doi:10.1029/2007JA012957.

Li, B., I. H. Cairns, and P. A. Robinson (2008b), Simulations of coronal type III solar radio bursts: 2. Dynamic spectrum for typical parameters, *J. Geophys. Res.*, *113*, A06105, doi:10.1029/2007JA012958.

Magelssen, G. R., and D. F. Smith (1977), Nonrelativistic electron stream propagation in the solar atmosphere and type III radio bursts, *Sol. Phys.*, *55*, 211.

Mann, G., F. Jansen, R. J. MacDowall, M. L. Kaiser, and R. G. Stone (1999), A heliospheric density model and type III radio bursts, *Astron. Astrophys.*, *348*, 614.

Meléndez, J. L., H. S. Sawant, F. C. R. Fernandes, and A. O. Benz (1999), Statistical analysis of high-frequency decimetric type III bursts, *Sol. Phys.*, *187*, 77.

Mitchell, J. J., I. H. Cairns, and P. A. Robinson (2003), New constraints and energy conversion efficiencies for plasma emission, *Phys. Plasmas*, *10*, 3315.

Mitchell, J. J., I. H. Cairns, and P. A. Robinson (2005), Conditions for plasma emission in the solar wind and very local interstellar medium (VLISM), *J. Geophys. Res.*, *110*, A11101, doi:10.1029/2005JA011267.

Paesold, G., A. O. Benz, K.-L. Klein, and N. Vilmer (2001), Spatial analysis of solar type III events associated with narrow band spikes at metric wavelengths, *Astron. Astrophys.*, *371*, 333.

Raulin, J.-P., and A. A. Pacini (2005), Solar radio emissions, *Adv. Space Res.*, *35*, 739.

Riddle, A. C. (1974), On the observation of scattered radio emission from sources in the solar corona, *Sol. Phys.*, *35*, 153.

Robinson, P. A. (1992), Clumpy Langmuir waves in type III radio sources, *Sol. Phys.*, *139*, 147.

Robinson, P. A., and A. O. Benz (2000), Bidirectional type III solar radio bursts, *Sol. Phys.*, *194*, 345.

Robinson, P. A., and I. H. Cairns (1993), Stochastic growth theory of type III solar radio emission, *Astrophys. J.*, *418*, 506.

Robinson, P. A., and I. H. Cairns (1998a), Fundamental and harmonic emission in type III solar radio bursts — I. Emission at a single location or frequency, *Sol. Phys.*, *181*, 363.

Robinson, P. A., and I. H. Cairns (1998b), Fundamental and harmonic emission in type III solar radio bursts — II. Dominant modes and dynamic spectra, *Sol. Phys.*, *181*, 395.

Robinson, P. A., and I. H. Cairns (1998c), Fundamental and harmonic emission in type III solar radio bursts — III. Heliocentric variation of interplanetary beam and source parameters, *Sol. Phys.*, *181*, 429.

Robinson, P. A., and D. L. Newman (1989), Quasiperiodic behavior in beam-driven strong Langmuir turbulence, *Phys. Fluids B*, *12*, 2319.

Robinson, P. A., I. H. Cairns, and D. A. Gurnett (1992), Connection between ambient density fluctuations and clumpy Langmuir waves in type III radio sources, *Astrophys. J.*, *387*, L101.

Robinson, P. A., I. H. Cairns, and D. A. Gurnett (1993), Clumpy Langmuir waves in type III radio sources — Comparison of stochastic-growth theory with observations, *Astrophys. J.*, *407*, 790.

Steinberg, J. L., M. Aubier-Giraud, Y. Leblanc, and A. Boischot (1971), Coronal scattering, absorption and refraction of solar radiobursts, *Astron. Astrophys.*, *10*, 362.

Suzuki, S., and G. A. Dulk (1985), Bursts of type III and type V, in *Solar Radiophysics*, edited by D. J. McLean and N. R. Labrum, p. 289, Cambridge Univ. Press, Cambridge, U. K.

Takakura, T., and H. Shibahashi (1976), Dynamics of a cloud of fast electrons travelling through the plasma, *Sol. Phys.*, *46*, 323.

Wild, J. P. (1950), Observations of the spectrum of high-intensity solar radiation at metre wavelengths. III. Isolated bursts, *Aust. J. Sci. Res. A*, *3*, 541.

Willes, A. J., P. A. Robinson, and D. B. Melrose (1996), Second harmonic electromagnetic emission via Langmuir wave coalescence, *Phys. Plasmas*, *3*, 149.

Willson, R. F. (1993), VLA-BATSE observations of an intense solar decimetric and hard X-ray bursts, *Astrophys. J.*, *413*, 798.

Xie, R. E., Q. J. Fu, M. Wang, and Y. Y. Liu (2000), The generation region of bidirectional electron beams in the corona, *Sol. Phys.*, *197*, 375.

Zheleznyakov, V. V., and V. V. Zaitsev (1970), The theory of type III solar radio bursts. II, *Sov. Astron.*, *14*, 250.

Ziebell, L. F., R. Gaelzer, and P. H. Yoon (2001), Nonlinear development of weak beam-plasma instability, *Phys. Plasmas*, *8*, 3982.

Ziebell, L. F., R. Gaelzer, and P. H. Yoon (2008), Dynamics of Langmuir wave decay in two dimensions, *Phys. Plasmas*, *15*, 032303, doi:10.1063/1.2844740.

I. H. Cairns, B. Li, and P. A. Robinson, School of Physics, University of Sydney, Sydney, NSW 2006, Australia. (cairns@physics.usyd.edu.au; boli@physics.usyd.edu.au; robinson@physics.usyd.edu.au)